Montanuniversität Leoben

Alloying of TiAlN single- and multi-layer thin films

Diploma Thesis

by

Jörg Radanitsch

Leoben, April 2009

This work has been carried out with CERATIZIT Austria G.m.b.H., Ceratizit Luxembourg S.á.r.l. and Materials Center Leoben Forschung G.m.b.H., at the Department of Physical Metallurgy and Materials Testing, Montanuniversität Leoben.

Affidavit

I declare in lieu of oath, that I wrote this thesis and performed the associated research by my self, using only literature cited in this volume.

Leoben, April 2009

_____

Jörg Radanitsch

Acknowledgements

I like to thank o. Univ.-Prof. DI. Dr. Helmut Clemens, Head of the Department of Physical Metallurgy and Materials Testing, for giving me the opportunity to carry out this work at his Institue.

Further I like to thank ao. Univ.-Prof. DI. Dr. Reinhold Ebner, Managing Director of the Materials Center Leoben, for giving me the opportunity to write this thesis within an MCL project.

Special thanks for kindness and expertise to ao. Univ.-Prof. DI. Dr. Christian Mitterer, Head of the Thin Film Group at the Department of Physical Metallurgy and Materials Testing.

Ten out of ten points for fun at work, scientific support and expertise go to my supervisor DI. Martin Pfeiler.

My deepest appreciation to DI. Dr. Martin Kathrein, CERATIZIT Austria G.m.b.H., DI Claude Michotte, CERATIZIT Luxembourg S.á.r.l., and the respective companies for their perfect support of this work.

Special thanks to DI. Dr. Gerardo Fontalvo of the Thin Film Group at the Department of Physical Metallurgy and Materials Testing, for expertise concerning tribological questions.

Furthermore I like to thank all my colleagues at the Department of Physical Metallurgy and Materials Testing and especially the Thin Film People.

Contents

1 Introduction

Today's research within thin film technology is carried out in various special fields for numerous applications. There are several unique requirements for those highly developed thin films. Customers demand better and of course cheaper products than competitors offer. For sure, it is not always the matter of costs that drives decisions as for high end applications, dependent on quality terms in the first sight and on costs in a second one. New materials somehow result in powerful impacts on society, while providing higher life standards and preserve ongoing prosperity. Keep on going ahead, thinking ahead and discussing future settings can provide sustainability for future generations.

Latest applications of physical vapour deposited thin solid films on cutting tools provide higher lifetimes under even worse conditions. Much higher hardness, better oxidation behaviour and other outstanding characteristics are reached by complex layer engineering. Precise controlled film growth and layer design are leading to more efficiency and less wear. Thin film applications, such as for special cutting tools, e.g. cutting inserts, are developed and tested on demand. Saving energy and resources is evident and a growing cost factor. Using less lubricants and coolants as one step towards decreasing energy consumption can be realized through protection of the tools from high temperatures by thermally isolating hard coatings. Thereby heat is kept inside the removed chips and less transmitted to the tool and the coating itself [1].

In case of cathodic arc evaporated TiAlN thin films, the enormous variety of alloying possibilities and the following modifications of the coatings' properties provide loads of coating systems to be investigated. The focus within this work was to find out more about the advantages that such alloyed TiAlN coatings could provide. Based on the ternary TiAlN films, used as a reference material, quarternary Ti-Al-X-N coating systems (X= B, Si, Ta, V) have been investigated in the form of single and multi-layer coatings. The comparison of those alloyed single and multi-layer coatings shall provide better understanding on the dominant effects and parameters, which are responsible for the coatings properties. Film architecture, alloying elements and bias voltage are taken into account as parameters that influence the coatings' properties. Investigations have been focused on structure analysis, mechanical properties, oxidation behaviour and wear. The structural analysis of the investigated coating materials shows the impact of the earlier mentioned parameters of influence on the different coating systems. Ongoing from the structural analysis further conclusions are drawn by evaluation of the mechanical properties in relation to structural changes of the single and multi-layer coatings. The hardness of hard coatings obviously is of major interest, while machining conditions and tool lifetime are often limited by hardness

values. Additionally to the hardness, the Young´s modulus and its regulation on demand is also of major interest within hard coatings design. Furthermore, the oxidation behaviour of thin films for high end applications plays an important role. The introduction of the mentioned quarternary coating systems by alloying of a fourth element is found as a useful approach to increase the oxidation resistance of these TiAlN based coatings. Oxide layer formation is observed under the focus to conclude on the oxidation resistance of the different coatings and again on their variations concerning alloying elements, bias voltage and layer architecture. Wear rates at room and high temperature conditions are investigated with tribological tests and calculations on the worn material bear a wear coefficient, which is used to find out positive and negative parameters of influence on the wear behaviour of the different coating systems.

2 Thin film fundamentals

2.1 PVD coatings

2.1.1 The PVD process in general

The physical vapour deposition process (PVD) is a well established technique to produce various types of functional thin film coatings. PVD thin films are deployed for optical-, decorative-, electronic-, thermal barrier and last but not at least wear resistant coatings. Each application requires specific film compositions and morphologies to reach the desired properties. To fulfill those requirements, various techniques have been developed since Thomas A. Edison started to get into this field of research in the late 19th century [2].
Generally, a metal vapour is produced out of a so called target material. The target material is the alloy which is deposited onto a substrate. The substrate can be made of all kinds of material that survives the process conditions of some hundred degrees and that fits into the sample storage system within the high vacuum chamber [3]. In case of cutting tool applications, the substrate is usually cemented carbide or high speed steel. The metallic vapour is transported from the target towards the substrate, where it condensates and forms the thin film layer. Additionally, reactive deposition processes can be applied. These processes work with reactive gases like e.g. oxygen, methane or nitrogen. The gases react with the vaporized target material which enables the formation of oxide, carbide, nitride, oxynitride or carbonitride thin films. The vaporization of a solid metal is in need of high energy and this can either be provided by the input of thermal energy or through mechanical impact energy [3, 4]. These principal differences of vaporization are leading to a certain classification into the basic PVD processes, as there are **Evaporation, Sputtering** and **Ion plating**. Figure 2.1 illustrates these processes and their principal mechanisms.

The evaporation technique

Evaporation, as shown in Fig. 2.1 a), uses *thermal energy* to vaporize the target material. This can be reached by either conductive or laser beam heating, electron beam or an arc discharge. Due to this more or less easy mode of operation, the evaporation process is important for various industrial applications. The evaporated particles (inside the high vacuum) have long mean free paths compared to the distance from the target to the substrate. Due to a gas pressure of ~ 10^{-3} to 10^{-6} Pa, there is little interaction between the particles through collisions, which leads to the generation of predominantly neutral atoms and just very few ions. In conventional evaporation, the vaporized metal particles with energies from 0.2 to 1 eV are condensing on the colder substrate and the chamber walls. Due to the relatively straight

movement, a so called “line in sight” transport of those particles is achieved, which makes it difficult to coat complex substrate geometries. The deposition rate of this process type is significantly better than observed for sputter deposition. Tailored film properties can be achieved by controlling the condensation conditions of the material to be deposited [3-6].

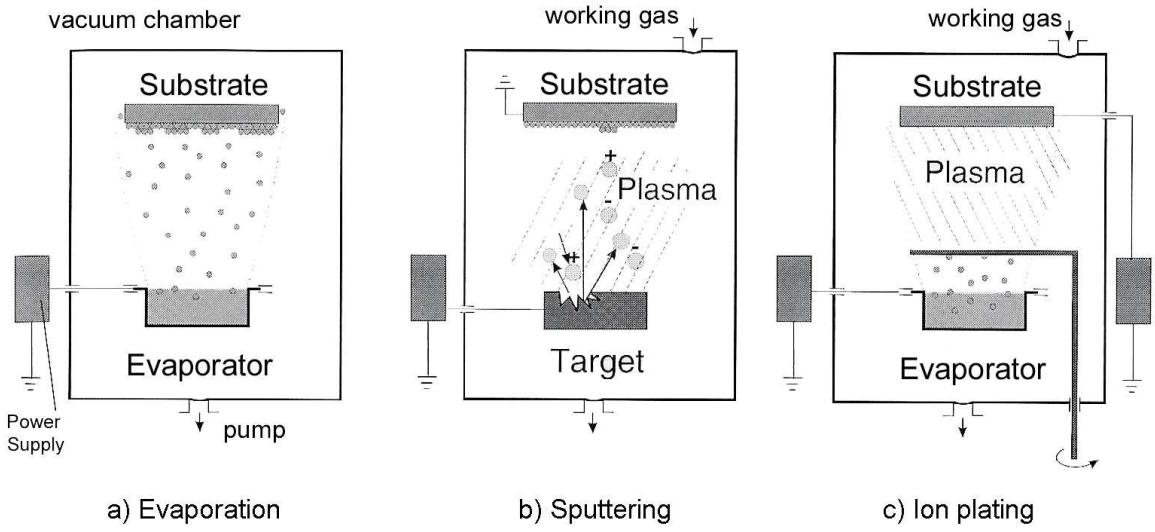

Fig. 2.1 The very basic PVD techniques [3].

The sputtering technique

Sputtering uses high energetic inert gas ion bombardment to evaporate the target material as shown schematically in Fig. 2.1 b). *Mechanical momentum transfer* from these impacting particles to surface atoms is responsible for sputtering. The necessary amount of energy to provide sublimation of the deposition material has to be provided by the kinetic energy of the impinging particles [4]. Generally, a high DC voltage (-1 to -5 kV) is applied to the target which is set as the cathode (-), while the substrate or the chamber walls act as anode (+). A pressure between 0.1 and 1 Pa guarantees interaction between the particles and ionisation thereof. This assembly leads to the ignition of a glow-discharge plasma in front of the target [3]. Positively charged Ar^+-ions from the plasma are accelerated towards the negative cathode, where they impinge and knock out atoms, ions or even clusters. The deposition rate is low compared to the evaporation process. Due to this economic disadvantage, the sputtering process has been enhanced to the *magnetron sputtering* technique. A permanent magnetic field is placed behind the target and forces the electrons to follow a longer and curved path on their journey towards the substrate. This guarantees higher collision rates, leading to higher ionisation rates of the inert gas atoms and an increase of the sputter rate by a factor of 5 to 10. As mentioned above, by application of reactive gases, the deposition of nitrides, oxides and

carbides is also possible, which then is referred to as *reactive sputtering*. Beside DC sputtering also high frequent alternating current sputtering is a common application for the deposition and is known as RF (*radio frequency*) or HF (*high frequency*) sputtering. The advantage is the possibility to deposit films of non conductive materials. The disadvantage of conventional sputtering without magnetron is the high temperature exposure of the substrate, which in the end is a factor of limitation [3-7].

The ion plating technique

Ion Plating (see Fig. 2.1) can be described as a technique related to evaporation or sputtering, because the evaporation can take place either as thermal evaporation or sputtering process. Important to note is that within the ion plating process a glow discharge is established to reach higher ionization rates of the vaporized species, which enables to govern the energy of the particles bombarding the substrate, and thereby to modify coating properties like mechanical properties and adhesion. Furthermore, this bombardment causes a surface cleaning or etching effect in the early stages of the process. Simultaneous occurrence of etching and redeposition of already eroded surface particles are leading to the formation of an interfacial layer that consists out of a mixture of film and substrate materials [5].

Glow discharge

Generally, glow discharge takes place when electric charge is transported between two electrodes through free electrons and ions within a gas or vapour [7]. Figure 2.2 illustrates the voltage to current characteristics at a certain working pressure and the related types of discharge to be distinguished.

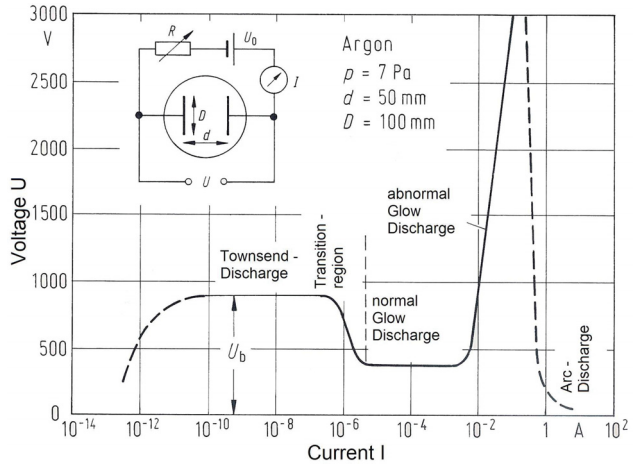

Fig.2.2 Voltage versus current, outlining different discharge regions [8].

Increasing the voltage causes a higher energy of the free electrons, provided through cosmic radiation or natural radioactivity. If the electron energies reach the ionization energy of the inert gas atoms, ionization of the inert gas atoms is taking place through inelastic collisions. Ions and electrons are generated. The ions are accelerated towards the negative electrode and hit the surface under production of further electrons (secondary electrons). All in all, loads of electrons are generated within the recipient and the current increases, while the voltage remains constant. This ionization is taking place avalanche like and is called *Townsend discharge.* Recombination of positive and negative charge carriers and collisions with the chamber walls decrease the ionized fraction present. A self sustaining glow discharge is reached when less recombination in order to creation of ions takes place. Thereby it does not matter if the ionisation is induced by collision of secondary or free electrons [6-10].
At higher currents the Townsend discharge is followed by the *normal glow discharge* area. It is characterized by a not entirely covered electrode surface by the plasma. The current is rising to high levels and shows a proportional behaviour to the covered electrode area, until the whole electrode area is covered. Most deposition processes with plasma as an ion source take place in the region of *abnormal glow discharge* where high voltage and high current densities are reached. The further increase of current results in formation of an *arc discharge* which exhibits very high currents and ionisation rates. This is one of the major benefits of the so called cathodic arc evaporation process, which will be explained detailed in the section below [3-9, 11].

2.1.2 The cathodic arc evaporation technique

The cathodic arc evaporation (CAE) process is a very important and wide spread method for large scale industrial hard coating deposition. This process can be related to the ion plating technique, while the evaporation of the target material is provided by an arc. The basic setup is displayed in Fig. 2.3 a). Generally, the target is set as cathode and the recipient acts as anode. The arc is ignited by contact between the cathode and a trigger wire. After ignition, the arc starts to move randomly and very quickly on its so called race track, which is a series of single arc spots on the target surface. This is referred to as *random arc*, which can be seen in Fig. 2.3 b).

a)

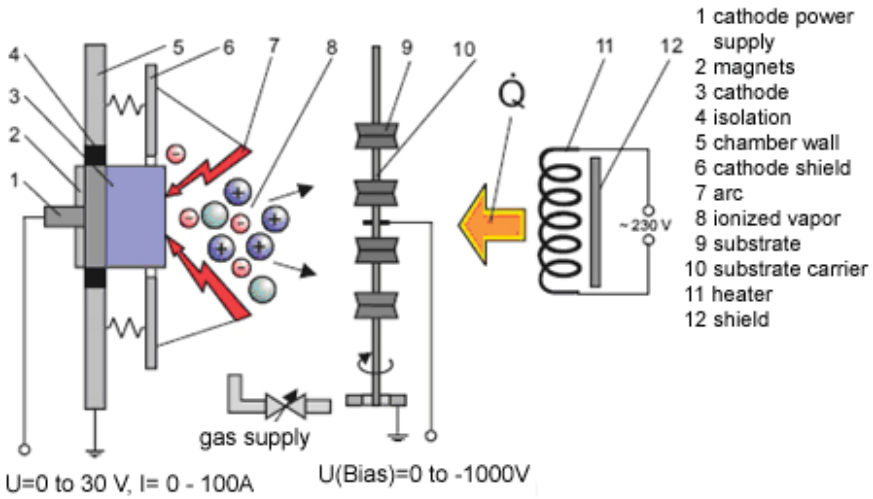

b)

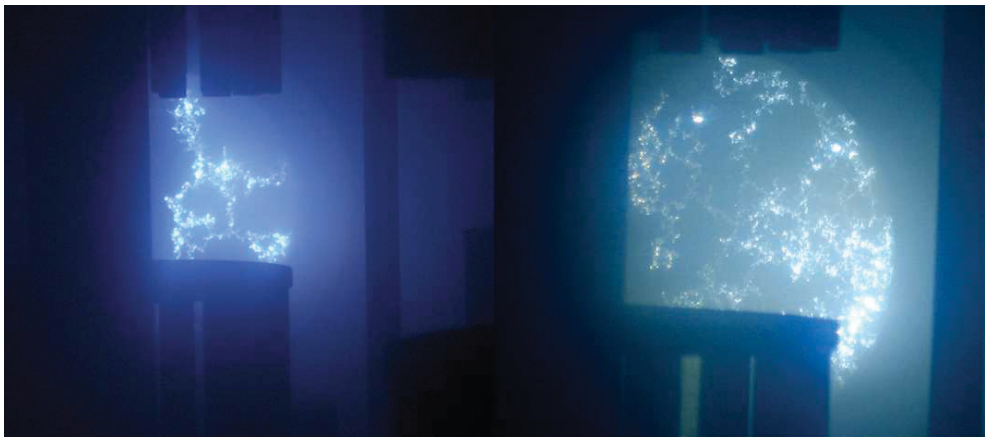

Fig. 2.3 a) The basic scheme of CAE [12], b) random arc movement, substrate holder in the front.

In order to provide homogeneous erosion and to avoid deep erosion grooves on the cathode (including the risk of leakage of the cooling system placed behind the target), dynamic magnetic fields are used to force the arc on a wanted race track. In this case, one is talking about a *steered arc*. The cathode is surrounded by an isolated confinement ring that keeps the arc within the target surface, not allowing it to hit the chamber walls. Figure 2.4 a) illustrates the homogeneous erosion through steered arc mode, while Fig. 2.4 b) is showing an unwanted concentration of the arc in the target centre and Fig. c) and d) deal with intermediate states of a) and b).

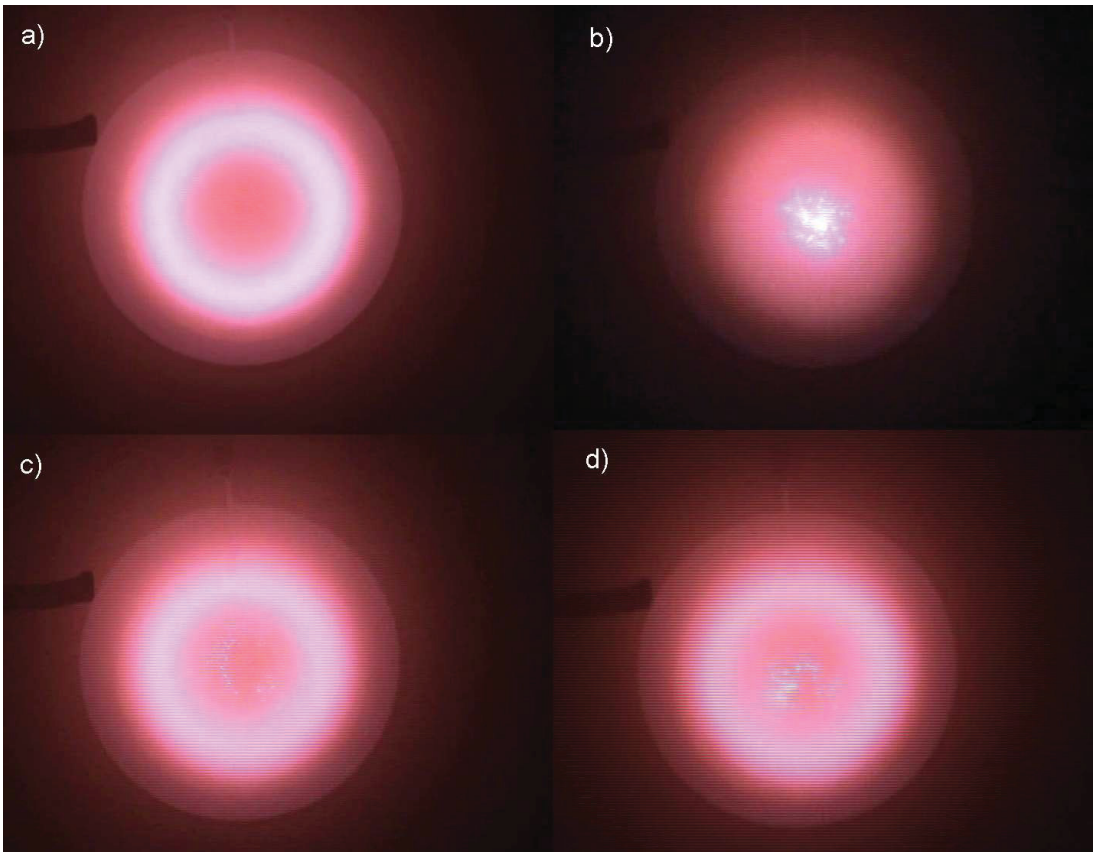

Fig. 2.4 Steered arc states, a) steered arc with homogeneous erosion, b) arc centered to the target, c) and d) intermediate states, showing fine arcs in the centre (modified [13]).

The arc evaporates the target material within a very small spot (2-50 µm in diameter) and the lifetime of one single arc spot is reported to be between 5 and 40 ns only. So, this shows how fast the arc moves around the target (10-200 m/s). Due to the use of currents between 40 and 300 A (compare Fig. 2.2), the spot is charged with very high power densities of 10^7 up to 10^9 W/cm^2 [4, 14]. This massive input of energy provides an almost instant evaporation and the high ionization rates of the vaporized target material. A resulting vapour pressure (~200 bar) in the arc spot crater ejects the plasma back inside the chamber, and a highly energetic and highly ionized particle flux called *plasma jet* is generated [7].
The ionization rate within the CAE process ranges from 50 to 100 % and the particle energies are found to be from 20 eV for light elements and up to 200 eV for heavy elements. Thus, a massive ion bombardment of the substrate takes place. First of all, this heavy ion bombardment cleans the surface and later on, a certain surface roughness is formed. This is called *ion etching*. Also atomic scale defects are created within the material due to the ion bombardment onto the surface, but surface roughness itself is believed to be the major reason for better adhesion of the deposited film [1].
Figure 2.5 shows the lifecycle of a single arc spot. A surface peak emits field electrons and due to its limited size, the tip is rapidly heated and quickly evaporated. The explosion like

evaporation of this surface tip and further field electron emission in combination with ongoing electron bombardment forms an erosion crater (Fig. 2.5 b), which is deepened and broadened through the vapour pressure mentioned above (Fig. 2.5 c). The formation of a new surface peak and molten metal particles are the consequences (Fig. 2.5 d). The new surface peak provides the next arc spot location (Fig. 2.5 e) [7].

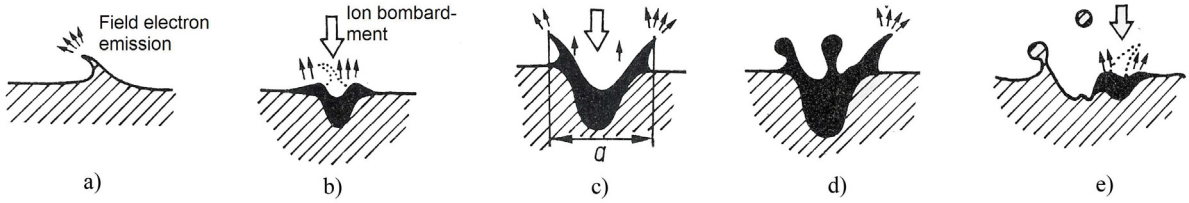

Fig. 2.5 Arc spot sequence on a cathode. a) field electron emission, b) explosion, melting, accelerating of molten metal. c) fully developed spot, d) shifting of the arc spot by a/2. e) creation of a new spot and droplet ejection (modified [7]).

A negative *bias voltage* is often applied to the substrate holder to accelerate the positively charged metal ions towards the substrate. Due to the influence on speed and ion energies through bias voltage appliance, the film morphology can be varied with changing the bias voltage [1, 4, 9, 10]. The high energy of the impacting particles leads to a higher mobility of the ad-atoms on the surface. This increase of the particle mobility shows a positive effect on the morphology and will be discussed more detailed later on. So, advanced film properties as good adhesion and density, are the result of these high particle energies and the above mentioned high ionization rates through CAE deposition [4]. Further influences on the arc spot movement are caused by the gas pressure inside the chamber and the type of the cathode material selected [4, 9, 10, 14].

A main disadvantage of CAE is the generation of macro particles. At the boundaries of the arc spot crater, so called droplets are dashed out of the surface and if they condense on the substrate, unwanted macro particles are formed (Fig. 2.5 e). These defects come from molten and not entirely vaporized particles. Those particles provoke an inhomogeneous film structure and thus mechanical properties are influenced negatively. Another harmful effect of the droplet induced roughness in CAE films is that those surfaces are less useful for decorative, optical or electrical coating applications [1, 4].
There are some methods to filter such macro particles from the plasma stream (electrons and ions are guided through a curved trajectory where droplets and neutrals cannot follow, slamming into the walls), but droplets are still a problem of cathodic arc evaporation in comparison to magnetron sputtering. So called FAD (filtered arc deposition) provides good results and allows arc evaporation to be used for electrical and optical coatings as well.

Another way to reduce the number of droplets is to speed up the arc spot movement, but all these techniques decrease the deposition rate. Finally, it can be summarized that the possibility to steer the arc spot, the high ionisation rate and the high deposition rate are the main advantages of the CAE process [1, 2, 4-7, 9, 10, 14].

2.2 Nucleation and growth of PVD thin films

Thin film nucleation is basically described with the heterogeneous nucleation on a substrate surface that varies in physical and chemical properties from the deposited material. Before nucleation can occur on the substrate surface, metal vapour particles have to be present on that surface. So, if those particles hit the substrate surface (Fig. 2.6) they can,

- be simply reflected,
- adsorbed (ad-atoms) and after some surface diffusion be desorbed again,
- or be adsorbed and form clusters with other ad-atoms or join existing ad-atom clusters.

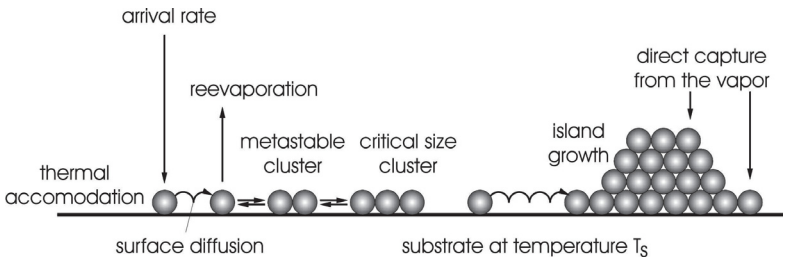

Fig 2.6 Processes occurring at 3-dimensonal nucleation leading to film growth [15].

Generally, the adsorbed atoms are more likely to diffuse on the substrate, because of their higher energy compared to the surface atoms themselves. More arriving vapour atoms gather with the ad-atoms and create clusters of a critical size, the so called nuclei. If once a nucleus is formed, the growth begins. Major parameters of influence on the nucleation are the *substrate temperature* and the *particle energies*, determining mobility and thus rearrangement of ad-atoms. Negative *bias voltage* accelerates positively charged particles towards the substrate and thus is used to adjust their energy on demand. The *gas pressure* inside the vacuum chamber is a further parameter of influence, while a higher gas pressure results in less kinetic energy due to an increased collision rate between gas atoms and condensed particles. The *angle* of the incident vapour particle flux is of main importance, while it causes shadowing at surface roughness or between grains (Fig. 2.8). Shadowed regions induce porous structures and generally weaken the films mechanical properties. Film structure

qualities as density and adhesion are set through variation of those principal process parameters [6-9, 16-18].

The nucleation and early thin film growth on substrates is described with three primary modes illustrated in Fig. 2.7. These are; island growth, layer by layer growth and finally the Stranski-Krastanov growth representing a combination of island and layer growth. Within *island growth (Volmer-Weber growth)*, a three dimensional island is growing from a nucleated cluster and is mostly observed when the film atoms themselves are bonded stronger to each other than to the surface atoms (Fig. 2.7 a). So it represents a typical type of growth for metal films on isolators. The *two dimensional layer by layer growth (Frank-Van der Merwe growth)* (Fig. 2.7 b) is especially related to films where the bonding between the atoms within the film and the substrate atoms is equal, or the bonding within the film atoms is even lower than between film and substrate atoms. As mentioned above the combination of these two modes is called the *Stranski-Krastanov growth* (Fig. 2.7 c). It starts with some two dimensional layers and with further distance from the substrate, the island growth becomes more favourable (Fig 2.7 c) [4, 7, 9, 16, 18].

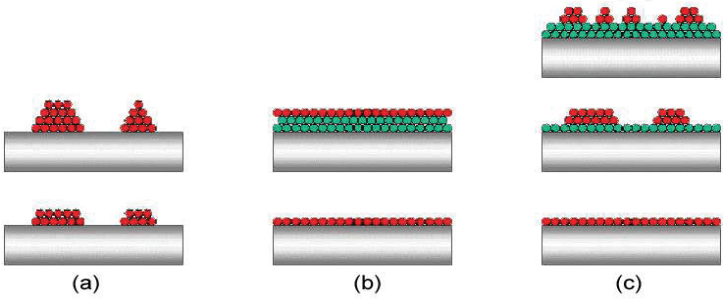

Fig. 2.7 Three basic modes of nucleation and growth of thin films. a) island growth (Volmer-Weber growth), b) two dimensional layer by layer growth (Frank-Van der Merwe growth) c) Stranski-Krastanov growth [19].

Except from those basic procedures of nucleation, there are some important aspects of thin film nucleation for applied processes. Generally, the first layers of atoms on the surface predict the morphology of the coating. The formation of a *transition zone* between substrate and coating depends on the process and the film particle reaction with the substrate. Basically, a layered transition, as described above, occurs within a few atomic layers if there is no diffusion or chemical reaction taking place between the substrate and the coating material, and if the vapour particles have low energies as e.g. described for the classical evaporation technique earlier. If chemical bindings can be formed between appropriate reactants as within

reactive techniques, the risk of brittle intermetallic phases being formed is evident. Such chemical reactions can lead to e.g. oxide layers which probably act as thermal barriers, or nitride layers that function as diffusion barriers [7, 9].

With the use of high energetic particles impinging on a substrate, as found in ion plating techniques, those particles can be implanted into the substrate material. This effect is additionally favoured by the earlier ion bombardment which causes defects that let the arriving particles diffuse inside the substrate material. The effect of bulk diffusion without previous damage can take place through mutual solubility of substrate and coating material. Thereby a continuous transition is formed which is favoured through high temperatures and longer times (this formation can even occur subsequently to the deposition process, e.g. within annealing) [7, 9].

The effect of *shadowing* occurs when the impinging particle flux does not cover surface or film areas placed behind obstacles. This leads to porosities, which can be diminished by higher particle mobility and time, as diffusing atoms can fill the shadowed areas and impede porosity (Fig 2.8 c). Anyway, practical applications end up in a combination of the mentioned nucleation effects, due to the process conditions chosen [4, 5, 7-9, 14].

After the formation of clusters during nucleation, the growth of various crystallographic directions takes place. Some of them are favoured to grow faster and others slower. This behaviour is related to the condensation rate of each crystallographic direction, depending on temperature, gas pressure and angle of the incident particles. Figure 2.8 a) shows zero surface diffusion and equal condensation rates for all orientations. Figure 2.8 b) also shows zero surface diffusion, but growth of favoured crystallographic orientations. Finally, the slower growing crystallographic orientations stop to grow, due to the lack of space already captured by the faster growing grains (Fig. 2.8 c). The phenomenon of repeating nucleation through very high mobility is displayed in Fig. 2.8 d).

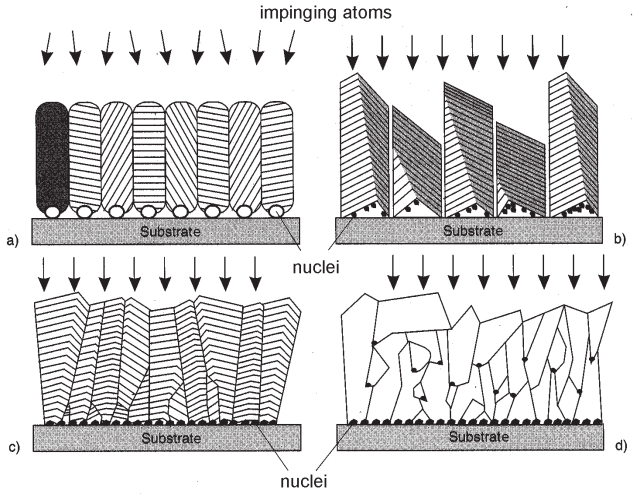

Fig. 2.8 a) Evenly growing columnar grains through diffuse angles of the incident particles. b) shadowing due to uneven growth of the crystallites, induced by fixed angle of incident particles. c) higher substrate temperature enables surface diffusion to fill shadowed areas and forms dense structures. d) repeating nucleation (modified [9]).

Generally, a cone like growth can be often observed as Fig. 2.9 illustrates. The increase of grain size with the growing film thickness can be compared to the structure displayed in Fig 2.8 c), where sufficient surface diffusion helps to form dense coating structures [1, 4-8, 11, 18, 20].

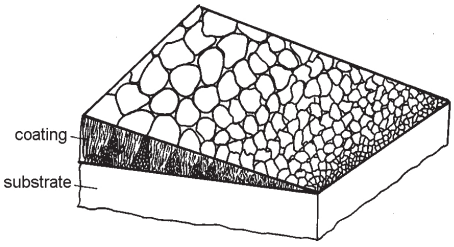

Fig 2.9 Grain size increase with growing film thickness (modified [7]).

2.3 Structure zone models and morphology

The correlation between structure and process parameters can be found in the so called structure zone models first published by Movchan and Demchinshin (Fig. 2.10) and later extended with a transition zone by Thornton and with the ion energy by Messier et al. Movchan and Demchinshin first were talking about three zones and showed that the temperature has a major influence on the film morphology. The melting temperature for many

pure metals is related to the activation energy for surface and bulk diffusion and so the homologous temperature is used in this structure zone model to show the relation between structure and the homologous temperature (T_s/T_m), T_s representing substrate temperature divided by melting temperature T_m of the target material [5, 9, 18].

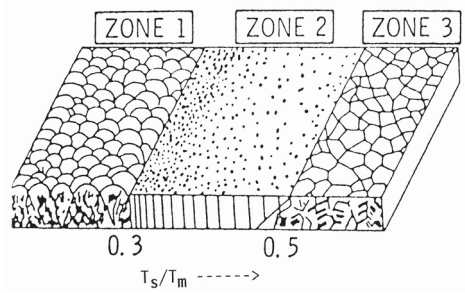

Fig 2.10 Structure zone model by Movchan and Demchinshin [7, 17].

Their first zone represents a porous zone with free standing columnar grains and a slightly rough surface with rounded grain tips, while the grain size increases with the distance from the surface. The porosity is related to *shadowing effects* which are consequently related to the low temperature and the particle immobility. Zone 1 represents the range of 0 to 0.3 times the homologous temperature and therefore the lowest temperature zone.
The second zone shows the effect of *surface diffusion*, which is now able to overcome the effect of shadowing to be the main influence on the morphology. Compared to the colder zone 1, zone 2 is formed at temperatures ranging between 0.3 and 0.5 of the homologous temperature. A dense structure is observed, forming a rather smooth surface on top. The grain size is increasing with higher temperature.
Zone 3 is representing very high temperatures providing enough mobility to let *bulk diffusion* take place. From 0.5 times of T_s/T_m, recrystallisation and renucleation can be observed while deposition is underway. This is leading to dense polycrystalline structures with bigger equiaxed grains.
This 3 zoned model does not describe the relation between morphology and any of the influencing process parameters except from the temperature. So, Thornton developed a model which is taking into account that for sputtering processes, higher energetic particles arrive at the substrate (4- 40 eV) and that the gas pressure inside the deposition chamber plays a role, due to the level of occurring collisions (Fig. 2.11 a.). Higher gas pressure leads to more collisions and particle energy drops. Thus, the ability for surface diffusion through the adsorbed particles is reduced and porosity is gained with higher pressure, as well as the structure zones are shifted to higher temperatures with higher argon pressures (Fig 2.11 a). This also defines the curved transition areas between the individual structure zones. Zone 1 then shows huge voids and a porous structure. A transition zone T is introduced which

consists of dense packed fibrous grains, due to enhanced surface diffusion (higher temperature). This zone is followed by the columnar grained zone 2 and the recrystallisation structure of zone 3. To avoid the big voids in zone 1 it is worth to apply a bias voltage as shown in Fig. 2.11 b). The stronger ion bombardment provides higher mobility, less surface roughness and more redistribution of film atoms. Those atoms can also fill voids and the higher mobility due to biasing also leads to better diffusion followed by increased nucleation. A decrease of voids in zone 1 is the consequence [1, 4, 5, 7, 9, 18, 20].

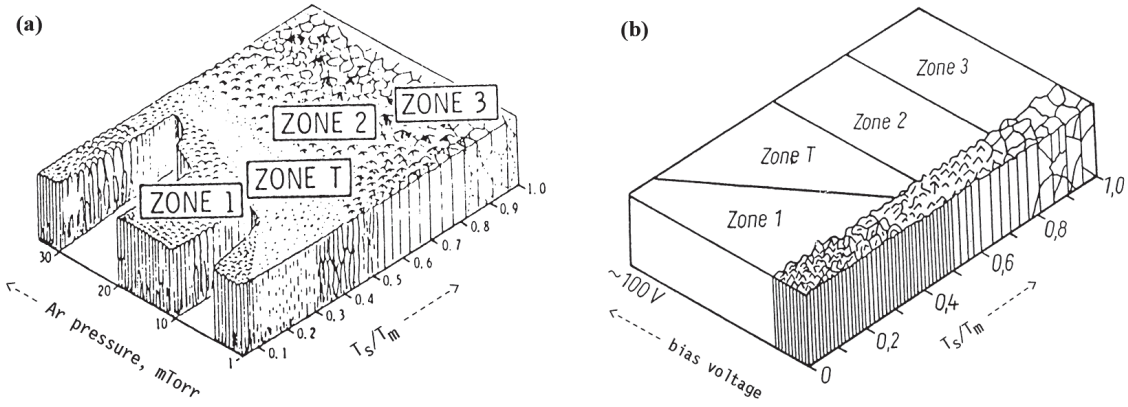

Fig. 2.11 a) Thornton and b) Messier´s structure zone models [21, 22].

The model after Messier et al. is of major importance for PVD processes using higher energetic particles of some ten electron volts as e.g. CAE does. Dense structures are realized at relatively low temperatures as surface diffusion is mainly provided by the particle energy and not through substrate temperature. Zone 1 is replaced by zone T for low temperatures and high bias voltages. Zone 2 and 3 are not heavily influenced by biasing because of the high temperatures with sufficient diffusion [1, 4, 5, 7, 9, 18, 20].

All the structure zone models describe that the effects of substrate temperature, gas pressure, impingement rate, the angle of incidence, substrate pre-treatment, high energy ion bombardment during deposition and the substrate bias voltage influence the film structure. As the models are developed for elemental metal films, a relation to more complex deposition situations as for multi component films is not easy. Different diffusion behaviour, ionization rates and varying melting temperatures of the alloyed elements must be taken into account [5, 7, 9, 14, 18, 23].

2.4 The basic coating system TiAlN

2.4.1 Aspects of TiAlN coatings

The use of cathodic arc evaporated TiAlN coatings is still increasing fast and has quickly replaced the former industrially deposited TiN for wear resistant cutting tool applications. Anyhow, TiN is a valuable material due to its bond structure as found within transition metal nitrides, consisting of metallic-, covalent-, and ionic bonding. This mixture causes high hardness, high wear resistance, chemical inertness, electrical conductivity and also superconducting behaviour is provided [1, 24].

The outstanding properties of TiAlN, especially when talking about oxidation and corrosion behaviour at elevated temperatures, were the driving forces for intensive research thereon. TiN oxidation starts at approximately 550 °C, TiAlN oxidizes far above this temperature [25]. Due to today´s demand of faster or less lubricated machining, those and higher temperatures are common process conditions. Special about the Al alloyed TiN is that it forms a protective oxide layer at elevated temperatures. This dense Al_2O_3 layer shows low thermal conductivity and prevents the tool below from excessive temperatures. Furthermore, it functions as a diffusion barrier and thus decreases diffusion wear.

Following the outstanding increase of its high temperature specifications, the TiAlN system has been well investigated. It was found that the high temperature improvements are related to the structure reached through alloying of Al to TiN, as the TiAlN system is a combination of the TiN and AlN system. TiN shows the face centered cubic (fcc) B1-structure which is also known as NaCl-structure, where Ti atoms settle the fcc lattice sites and the small N atoms are sitting on the octahedral sites in between. AlN exhibits a hexagonal close packed (hcp) structure, representing the B4 wurtzite or ZnS structure, with Al atoms on the hexagonal lattice sites and the smaller N atoms within the tetrahedral sites. Now, if Al is alloyed to TiN, the Al atoms substitute the Ti atoms and so the fcc structure of TiN is maintained, at least for certain Al contents (Fig. 2.12) [1, 14, 23, 25-27].

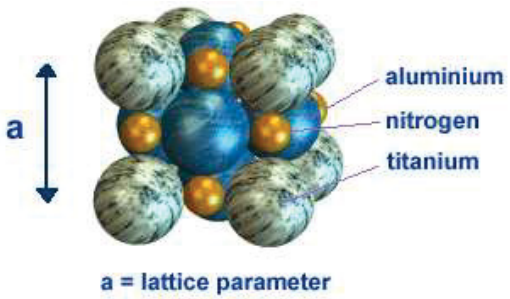

Fig. 2.12 NaCl/B1 lattice structure for TiAlN with nitrogen on octahedral sites (modified [28]).

The quasi binary phase diagram of TiN and AlN in Fig. 2.13 b) shows that there is just low solubility for AlN within TiN and vice versa. One can see that the maximum solubility for AlN (~5 %) is reached at a very high temperature of approximately 2700 K. The wide and predominant two phase area consisting of cubic TiN and hexagonal AlN represents an equilibrium composition within this system. Following this phase diagram, there should be a two phase area for common temperatures between 300 °C and 500 °C of CAE deposition processes. However, a supersaturated metastable cubic solid solution (TiAlN) is found to be present within this temperature zone (Fig. 2.13 a). The reason for this supersaturation behaviour can be related to the high energy of the deposited particles and low substrate temperature, leading to the metastable fcc TiAlN solid solution [1, 23, 25-27, 29].

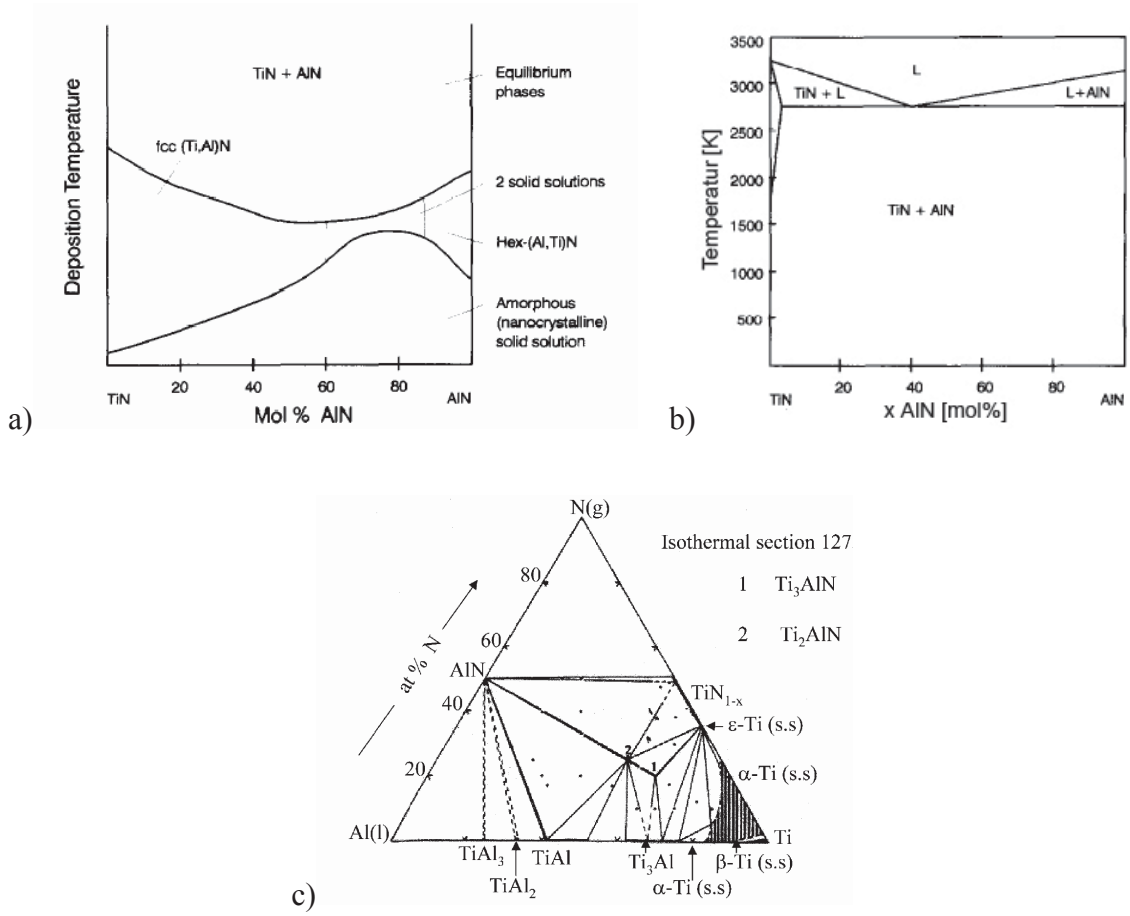

Fig.2.13 a) TiN-AlN PVD phase diagram showing phase formation under thermal non equilibrium conditions [23]. b) quasi binary TiN-AlN phase diagram [23] c) ternary phase diagram of Ti-Al-N at 1273 K [1].

The isothermal ternary phase diagram of Ti, Al and N shows two phases in thermodynamic equilibrium at 1000 °C (Fig 2.10 c). Those two phases are the cubic B2 perovskite structure (Ti_3AlN) and the hexagonal H-phase (Ti_2AlN) phase.

As mentioned above, the smaller Al atoms substitute the bigger Ti atoms and lead to a decrease of the lattice parameter. This causes elastic deformation and strengthening of the metastable fcc lattice. The content of Al influences the lattice structure and it was found that for Al contents beyond 70 % the structure changes from the fcc NaCl to the hcp ZnS structure. In the region of 60 to 70 % Al, a transition zone with coexisting fcc and hcp phases is found. Several authors report slightly varying values within this range of Al content, depending on the process conditions observed. Spencer et al. made thermodynamic calculations [30] and Kimura et al. reported on an experimental approach to define this transition zone within the TiN-AlN system [27].
Consequently at 100 % AlN content, the hexagonal AlN structure is reached. Figure 2.14 illustrates this relation of the Al-content on the structure, from the fcc TiN to the two phase region of fcc and hcp TiAlN ongoing to the pure hcp AlN structure [1, 14, 23, 26, 27, 31, 32].

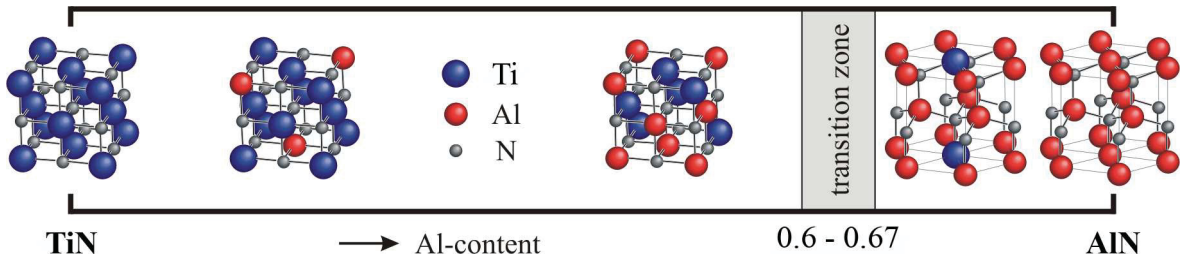

Fig 2.14 Relation between Al-content and crystal structure [33, 34].

2.4.2 Effects of bias voltage and ionization rate

Due to the earlier mentioned effect of bias voltage to influence the particle impact energy, it is a process parameter of major importance. One effect caused through biasing is an intensified ion bombardment, which leads to a higher lattice defect density and thus to higher compressive stresses (Fig. 2.15 a) [35]. But higher bias voltage also brings in higher mobility and defects can anneal, which decreases residual stresses. The predominance of this annealing effect has been observed to be present for bias voltages below -150 V only [36].

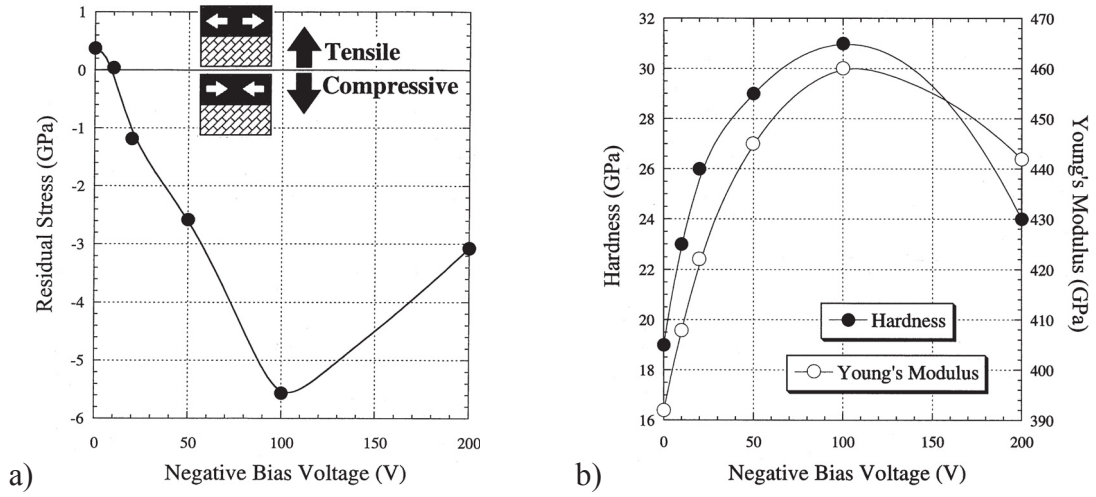

Fig.2.15 a) Correlation between bias voltage and residual stresses, b) hardness and Young´s modulus versus bias voltage [35].

For alloyed targets as e.g. TiAl for coatings, Ti and Al differ in their ionisation rate and degree. Thus they are not equally attracted to the substrate by bias. The ongoing ion bombardment onto the deposited film can lead to resputtering thereof. As far as Al ions have a higher rate of resputtering compared to Ti ions, higher bias voltage leads to less Al content within TiAlN coatings. Thus bias voltage can lead to a significant difference in composition between target and coating [24, 35]. Anyway, experimental results of TiAlN multi component films show a corresponding structure at lower substrate temperatures as observed for elemental films deposited [23, 37]. Sato et al. reported that the increase of hardness is related to the higher ion bombardment and the thereby induced residual compressive stresses (Fig. 2.15 b). This has been observed for bias voltages up to -100 V, while at higher bias values the hardness decreases again [35].

Another major effect caused by biasing is the change of texture. Increasing ion energies have been observed to be related to the change of texture from (111) to a (200) orientation [38]. In case of V alloyed TiAlN coatings, Pfeiler et al. mentioned a structural response on bias voltage appliance and variation. Thereby the formation of the hcp phase is hindered through higher bias voltages. Introduction of bias voltages of -40 V showed coexisting hcp and fcc phases, while increasing bias voltage (-160 V) led to a single fcc phase, which caused a significant increase of hardness and Young´s modulus [39]. Generally, the variation of bias voltage is a smart way to control process conditions and their influence on coating structure and morphology, leading to advanced properties.

2.4.3 High temperature behaviour of TiAlN

As mentioned above, TiAlN is seen as a further development of the successful TiN for high temperature applications. In case of required thermal stability as for milling, it can be found that TiAlN reaches a certain point, where decomposition of the metastable phase into its equilibrium phases occurs. An experimental approach through annealing carried out by Hörling et al. shows that at 900 °C, fcc AlN precipitates from the metastable supersaturated matrix [40]:

$$\textbf{fcc-TiAlN} \rightarrow \textbf{fcc-TiN} + \textbf{fcc-AlN}$$

At elevated temperatures of 1100-1250°C, fcc AlN is able to transform into hcp AlN:

$$\textbf{fcc-AlN} \rightarrow \textbf{hcp-AlN}$$

The entire transformation is:

$$\textbf{fcc-TiAlN} \rightarrow \textbf{fcc-TiN} + \textbf{fcc-AlN} \rightarrow \textbf{fcc-TiN hcp-AlN}$$

This transformation is related to spinodal decomposition, due to energetic advantages for the supersaturated system. The formation of hcp AlN needs more energy, because of incoherent interfaces with the neighbouring TiN and a bigger unit cell that must be established [40]. As the formation of fcc AlN is aligned to a lower effort of energy, this intermediate step during decomposition is observed. Mayerhofer et al. investigated the spinodal decomposition via Differential Scanning Calorimetry (DSC) and showed that an increase in hardness takes place when the coherent fcc AlN phase is formed at 600-1000 °C, which confirms precipitation hardening within the TiAlN system. Consequently, the hardness decreases when the incoherent, hexagonal AlN equilibrium phase precipitates at temperatures above 1000 °C [41].

2.4.4 Mechanical properties

In general, the deposition process and its parameters influence the occurrence of the maximum hardness. The Al content and thus the phase composition of the film has got a major impact on its mechanical properties. Figure 2. 16 b) illustrates the relation of Al content versus hardness and Young´s modulus. With an increasing Al content the hardness increases due to solid solution hardening. The more Al atoms substitute the bigger Ti atoms inside the TiN lattice, the more elastic strain occurs. As long as the single phase metastable fcc structure

is present, hardness rises with the Al content. When the solubility of the fcc lattice for Al is depleted, hcp phases form and represent fractions of lower hardness, decreasing the hardness of the two phase material (Fig. 2.16 a). Also the Young´s modulus increases as the hardness with rising Al contents and decreases quickly if the hcp phase appears [1, 32].

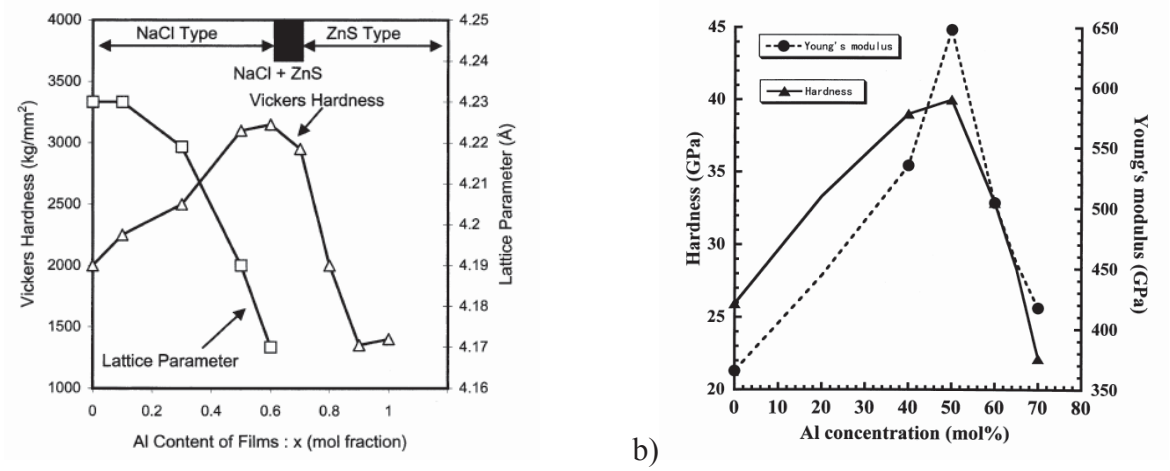

Fig. 2.16 a) Vickers hardness dependence on Al content and structure, change of lattice parameter of the fcc phase while alloyed [1]. b) Al concentration vs. hardness and Young´s modulus [32].

2.4.5 Tribological behaviour

Scientific reseach on the origins of friction has a long history since Leonardo da Vinci already mentioned the proportionality of normal force and limiting friction force in the late 15th century [42]. Anyway, compared to mechanics, thermodynamics and plasticity, tribology itself is a very new field of science, since the lion´s share of knowledge was gained after the Second World War. Tribology is a derivate of the greek word “tribos”, meaning sliding or rubbing. Wear is the principal reason for materials to be wasted and for loss of mechanical and geometrical characteristics. Wear is omnipresent in technical questions and tribology is the science that investigates and solves related problems. Wear is further distinguished into the forms of adhesive-, abrasive-, fatigue-, erosive-, cavitation-, corrosive-, oxidative-, fretting-, melting-, impact- and finally diffusive wear [42]. Friction instead is energy dissipation. Approximately one third of the energy used can be related to be “lost” through friction [42]. It is important to mention that friction and wear are two individual phenomena and that they are not necessarily related to each other. High wear might be deserved under low friction, if lubricants are provided by the material itself, e.g. in self adaptive coatings [43, 44]. Furthermore, low wear might be seen in connection with high coefficient of friction.

The wear resistance of TiAlN is determined through hardness, micro structure and the ratio of Ti/Al. PalDey et al. mentioned high hardness to be beneficial in abrasive wear resistance at elevated temperatures between 300 and up to 1000 °C, being faced by cutting tools. It was shown that TiAlN and TiN coatings have a much higher friction coefficient (1-1.2) as observed for Ti(C,N) (0.1-0.2) [1, 45].

For room temperature and dry sliding conditions, the wear rate is influenced by the Al content and increases with Al addition to the coating material. Contrary to reported cutting tests, in tribological tests although hardness and Young´s modulus are increasing with higher Al content, the wear rate increases as well. This could be connected to the decrease of the shear modulus. More shear causes more wear [46]. Another possible effect is that harder coatings can lead to a higher impact of the friction load due to a smaller bearing surface than for ductile materials. The consequence is massive plastic deformation on a very small area. This leads to fatigue at the highly loaded spot, which results in the generation of small abrasive particles. Consequently, the wear rate increases [39, 46, 47]. Furthermore, the structural transformation from fcc to the structure consisting of fcc and hcp phases (at higher Al contents), leads to a higher wear rate caused by the reduced hardness. In case of cathodic arc evaporation, the high droplet density, in comparison to sputtering deposition, has a negative influence on the wear rate [1, 48-50].

All these influences on the thin films wear illustrate how diverse the operating conditions affect the coatings wear resistance and that generalized conclusions are difficult to make. However, there is always the need to determine which parameters are driving forces regarding to the wear behaviour of the material in use. For high temperatures, TiAlN is definitely superior in wear resistance than TiN, as oxidation comes in to play.

2.4.6 Oxidation behaviour

If the oxidation behaviour of TiAlN is compared to TiN, it has been proved by several authors that the Al content inside the TiN lattice provides a much higher oxidation resistance at temperatures higher than 600 °C. Common temperatures for cutting applications are found to be within a range of 500 to 1000 °C. The TiAlN coatings are providing good oxidation resistance up to ~800 °C. The initiation of oxidation is observed quite lower at approximately 700 °C. So, the range of the oxidation initiation temperature depends on the Al content as well as on the microstructure (Fig. 2.17). As mentioned earlier, a dense oxide top layer of corundum (α-Al_2O_3) is formed on the surface of the TiAlN coating at high temperatures. A main advantage of this oxide layer is found within its function as a diffusion barrier. Thus,

diffusion is hindered in both directions through the oxide layer. Diffusion wear is an important form of wear within high temperature use of cutting tools [1, 51-53].

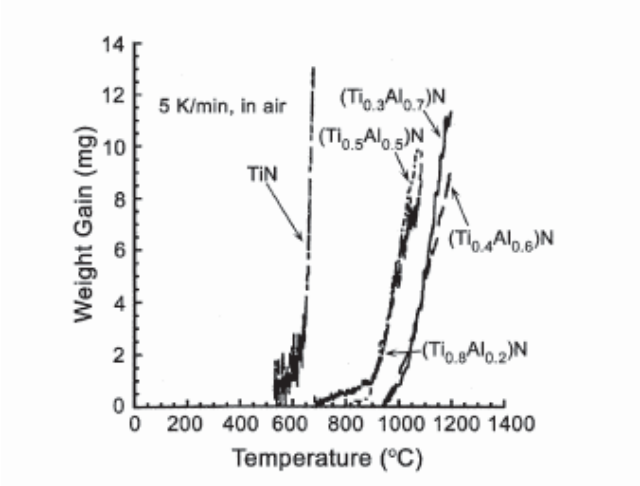

Fig 2.17 Oxidation behaviour related to the Al content [32].

As an example of a high temperature oxide layer on a quaternary Ti-Al-V-N coating, Fig. 2.18 illustrates bulk material, interlayer, coating and the oxide layer on top. Droplets and their destructive behaviour can be seen as well. The oxide diffusion barrier layer is disturbed in the area of droplets and as a consequence, diffusion is favoured in those macroparticle surroundings. The “bubbles” on top of the coatings surface and in the near background of the image are probably caused by preferred oxidation of droplet generated surface roughness tips.

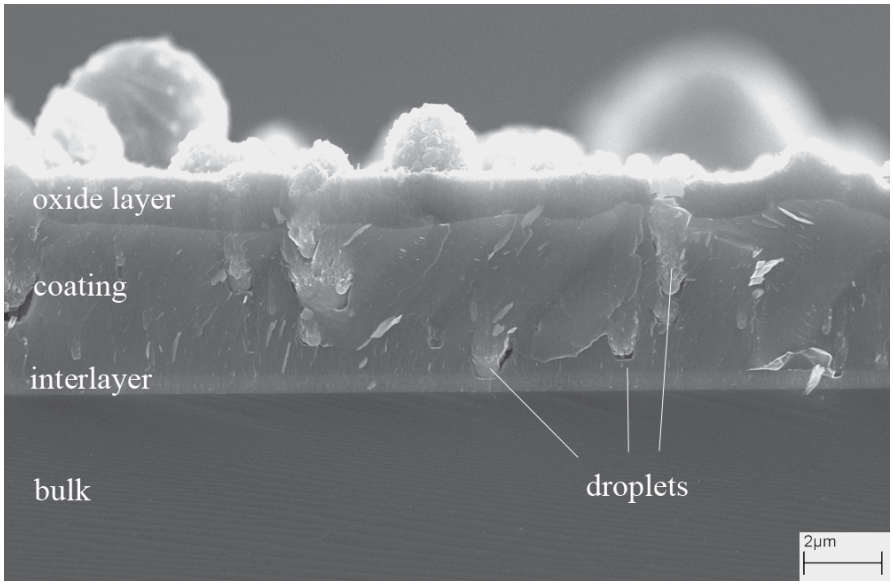

Fig. 2.18 Scanning electron microscope cross section of a Ti-Al-V-N coating.

2.4.7 Alloying of TiAlN coatings

Further development of TiAlN is focused on enhancing its properties to further dimensions. Alloying and therefore creating new ternary or quaternary systems, opens new perspectives for wear resistant thin films. There are several elements which have been alloyed to the basic systems of TiN and TiAlN to meet the required application properties of modern machining.
To improve the oxidation resistance, Cr (3 %) and Y (2 %) can be added. Y also causes grain refinement and lowers the residual stresses [1]. Furthermore, Y supports the formation of hcp-AlN and as hardness (H) and Young´s modulus (YM) values for the hcp phase are lower than for the cubic phase, H and YM drop with higher Y contents [54]. Zr is known to stabilize the fcc TiAlN structure and to form a thin oxide layer which can be compared to Al_2O_3. Both effects increase the wear resistance. Another important alloying element is V, which is reported to improve hardness, and to lower ductility with higher contents (solid solution hardening). The fcc lattice is also stabilized by V and thus more Al can be alloyed to TiAlN, respectively, leading to higher hardness. V can also lead to formation of lubricious oxides at higher temperatures [44]. Si generally increases hardness and decreases chemical reactivity of the coating, due to its chemical inertness. Durand-Drouhin et al. line out the increasing hardness and that the elastic modulus is not affected notably. They claim the Hall Petch effect to be responsible for that behaviour. Ti-Al-Si-N has a smaller grain size than TiAlN [55]. Si is also known to lead to the formation of so called nano-composites, where nonocrystalline TiAlN is surrounded by an amorphous tissue phase of Si_3N_4 [56]. Similar reports have been made for B alloyed systems by Barker et al. [57]
In case of improved abrasive wear, B has proven its beneficial effects. It increases abrasive wear behaviour due to self lubricating effects, depending on the structure (h-BN). If cubic BN is formed, the hardness is improved as well. The relation between Al and B content is reported to be important for the dry wear properties [1, 58]. Ta also is one of the alloying elements that stabilizes the fcc phase, and thus is leading to increased wear resistance and better mechanical properties. An increase of the maximum milling time of 20 % compared to TiAlN coatings is reported. Pfeiler et al. mention that a protective oxide layer might be formed at high temperatures. For high temperature applications, Ta alloyed TiAlN coatings can be seen as highly wear resistant, as the oxidation rate is diminished [59, 60].

2.4.8 TiAlN multi-layer coatings

Further improvements of hard coatings have been reached through the formation of multi-layer thin films. Figure 2.19 illustrates coating configurations of single-, bi-, multi- and nanolayer films. Within multi-layer coatings, alternating layers of certain compounds are formed within usual deposition processes. Multi-layer structures show a further increase in

mechanical properties as hardness and strength compared to the mentioned ternary or quaternary single layer coatings. This can be related to the massive increase of interfaces within the film and the resulting dislocation pile up thereon [61]. The thickness of each layer is for example set through the deposition rate and the rotation speed of the substrate holder inside the recipient. The smaller the layers, the more interfaces are generated. If very small periods are present, one is talking about superlattice or nanolayer coatings. These coatings tend to be the hardest films by now and are called "super hard coatings" (more than 40 GPa). The high amount of interfaces is responsible for the outstanding mechanical properties. Each layer is in nanometer scale (5-10 nm) of thickness [1, 62, 63].

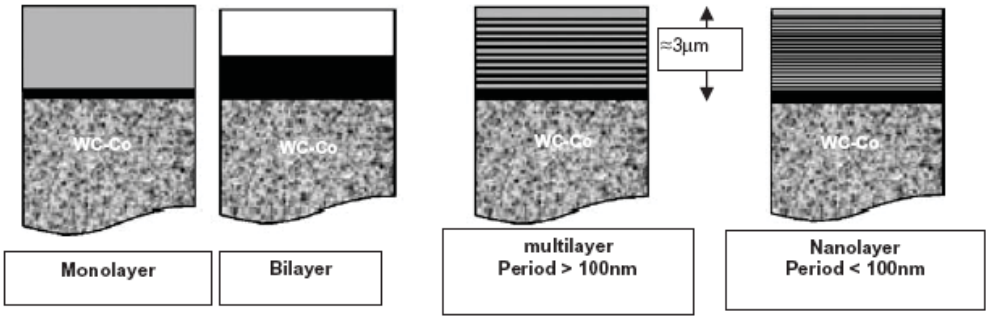

Fig. 2.19 Different coating configurations, overall layer thickness remains at 3 µm [62].

Han et al. report that the hardness and lattice parameters of TiAlN/(Ti,Al)CN multi-layer coatings can be found to be in the middle of the values of the two single components TiAlN and (Ti,Al)CN. Also the multi-layer coatings adhesion is found to be better than for single layer coatings. Another present advantage is a superior impact failure resistance of multi-layer coatings [64].

However, the effect of increasing hardness through multi-layer deposition has also been proved if just one layer type is deposited in a multi-layer form TiAlN/TiAlN. [1, 65]. The distance for two repeating layers is written as modulation wavelength λ and is therefore related to the layers thickness. The grain size is determined by the thin layers thickness and also the typical columnar grain structure can not be formed due to a lack of space. A major increase of hardness is observed. So, this hardness increase is not mainly depending on the layer material chosen to deposit, but it is dependent on the structure reached through multi-layer thin film design [1, 66].

3 Experimental details

3.1 Deposition equipment and process parameters

All investigated samples within this project have been coated by CERATIZIT Luxembourg within an industrial scaled PVD facility. An Oerlikon-Balzers Rapid Coating System (RCS 900) was used. Figure 3.1 illustrates the deposition facility, the chamber layout concerning the possible arrangements of targets and substrates, as well as the location of the resistance heating devices. There are six possibilities to mount targets within this type of coating recipient. Two Ti targets are necessary to deposit the TiN interlayer at the beginning of the deposition process. Subsequently, the alloyed target material is evaporated. In case of single layer deposition, four targets of the desired alloy to be deposited are mounted and in case of multi-layer coatings, two and two targets of the alternating film materials are mounted. Multi-layered films are reached through rotation of the substrates.

a) 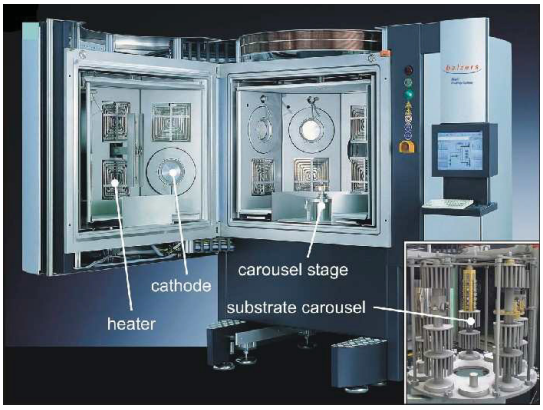

b) 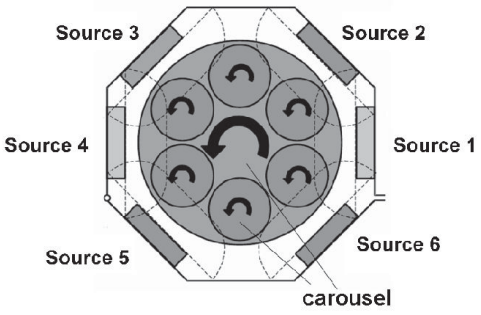

Fig 3.1 a) Recipient with locations of heater, cathodes (targets), carousel (modified [33]) and b) schematic configuration within an Oerlikon-Balzers RCS 900 machine, targets are placed in source locations and substrates on the carrousel in the middle (modified [67]).

To provide maximum compatibility of processing between consumer products and the researched coatings, all process steps have been carried out as in daily deposition routines.
First of all, the substrates are cleaned with acetone and ethanol in an ultrasonic bath. Then the loaded substrate holder carousel is placed inside the recipient. Generally, the deposition process starts with the *evacuation* of the chamber, where pressures of 10^{-5} mbar are reached. As a second step, *heating* up to 450 °C was set for the present work. Heating is provided through inductive heaters and through electron bombardment. An electron source on top of the chamber provides the electrons which impact on the (in this step) anodic substrates and cause heating through energy transfer. To make the sample surface ready for the deposition

process, another cleaning step known as *ion etching* is performed. There, a plasma is ignited to act as an ion source. The substrates are now set as cathode, the recipient as anode and the inert argon gas provides atoms to be ionized. These ions clean the substrate surface. The *deposition* starts with nitrogen as a reactive gas and the ignition of the two Ti targets for the TiN interlayer, followed by deposition with the alloyed targets. During deposition a N_2 atmosphere is present at a working pressure of $3.2*10^{-2}$ mbar. All in all the deposition takes six hours. After cooling the whole system down, the samples are unloaded. The single and multi-layered thin films have been produced as versions with -40 V and -80 V bias voltage. Table 3.1 shows an overview of the coating systems produced.

Tab. 3.1 Investigated coatings, composition in at. %.

a.) 5 single layer designs.

$Ti_{32.9}Al_{67}B_{0.1}N$	$Ti_{31.7}Al_{63.3}Ta_5N$	$Ti_{32.5}Al_{67}Si_{0.5}N$	$Ti_{16.5}Al_{67}V_{16.5}N$	$Ti_8Al_{67}V_{25}N$

b.) 5 alternating multi-layer designs.

$Ti_{32.9}Al_{67}B_{0.1}N$	$Ti_{31.7}Al_{63.3}Ta_5N$	$Ti_{32.5}Al_{67}Si_{0.5}N$	$Ti_{16.5}Al_{67}V_{16.5}N$	$Ti_8Al_{67}V_{25}N$
$Ti_{50}Al_{50}N$	$Ti_{50}Al_{50}N$	$Ti_{50}Al_{50}N$	$Ti_{50}Al_{50}N$	$Ti_{50}Al_{50}N$

3.2 Thin film characterization techniques

3.2.1.1 Samples

A variety of samples has been coated within each deposition run, while each deposition run represents the different alloys and the varying bias conditions. The different sample materials listed below, i.e. silicon (Si) and cemented carbide (CC) are related to the diverse forms of thin film materials characterization.

- Si wavers for heat treatments and X-ray diffraction.
- CC-SNUN plates for hardness and Young´s modulus evaluation.
- CC-discs for tribological investigations.
- CC-SEKN plates for machining tests.

3.2.2 Film thickness and light optical microscopy analysis

To measure film thickness, the ball crater technique (CSM Calo-Test) was used. With a diamond suspension, a ball grinds a spherical wear crater throughout the entire coating. This provides an insight to the substrate, the interlayer and the investigated coating. Observing this crater within a Reichert Polyvar MET optical microscope and finally characterizing the craters diameters with the ANALYSIS software, the films thickness can be calculated.

3.2.3 Heat treatment and oxide film formation

The coatings on Si wavers have been oxidized in air at two different conditions. This procedure has been chosen due to the varying behaviour of V alloyed samples showing lower oxidation resistance. The size of the Si wavers has been reduced to pieces of 7 x 5 x 0.39 mm each. All samples except those containing V have been annealed at 900 °C for 1 hour within a Carbolite RHF 16/15 furnace. The V containing samples have been annealed at 650 °C for 30 min within a Carbolite HRF 7/45 furnace. Both ovens have been set with a heating ramp of 10 K/min, followed by the given holding time of 60 or 30 min before the samples have simply been cooled down inside the furnace. The aim of annealing is related to illuminate of oxide layer formation and therefore fracture cross sections of this heat treated samples have been prepared.

3.2.4 Scanning electron microscopy

Scanning electron microscopy (SEM) was used to measure the oxide layer thickness after annealing tests, offering valuable information about coating zones and structure, as well as about droplet appearance. A reference material with the as deposited state has been investigated as well. The Si samples have been broken and micrographs were taken from the fracture cross sections. The pictures have been taken with secondary electron (SE) and back scattered electron (BSE) detector methods. Secondary electrons have lower energy (0-50 eV) in comparison to backscattered electrons which have energies far above 50 eV. The SE carry surface near information which results in higher contrast and surface topography of the images. BSE´s show up with more information of the substrate, which leads to less contrasted pictures with respect to surface topography but with the benefit of elemental contrast (Fig. 3.2).

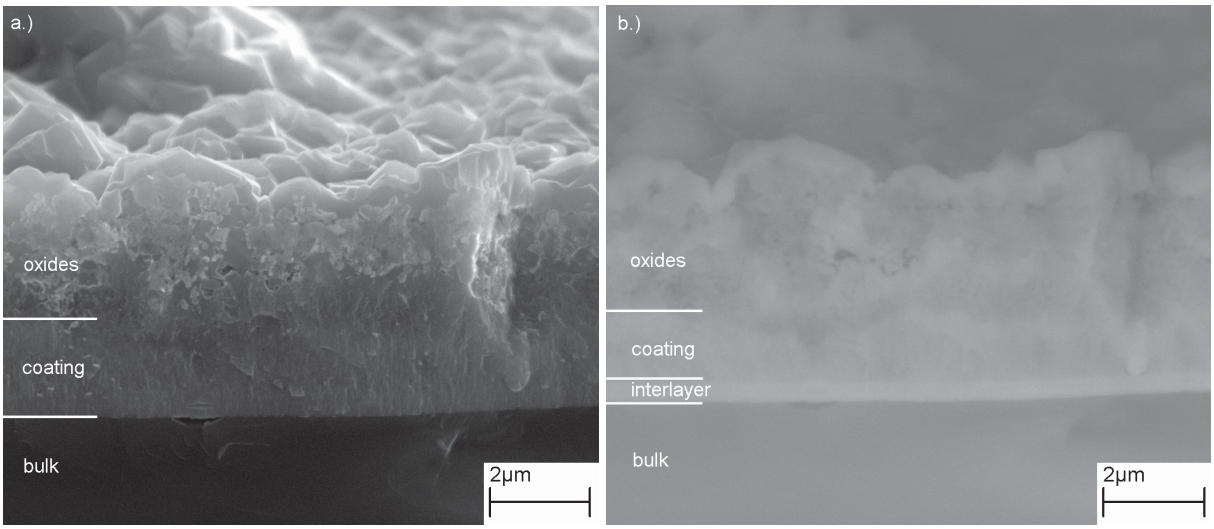

Fig 3.2 Image a) shows a SE picture and image b) a BSE picture. BSE makes e.g. the TiN interlayer more visible.

3.2.5 X-ray diffraction

X-ray diffraction (XRD) is used to investigate the coatings structural composition through detection of diffracted X-rays at atomic layers. Furthermore textures, grain size and residual stresses can be measured with this technique. Cullity et al. reports on the modification of the diffraction peaks due to changes of internal stresses and grain sizes, compared to virgin material [68]. Figure 3.3 shows the principle of this diffraction mechanism and how the so called *Bragg´s law* must be fulfilled to obtain peaks in an XRD pattern. Thereby, *d* describes the lattice spacing, λ the wavelength of the X-rays, θ the diffraction angle (cf. Fig. 3.3) and, *n* finally describes the class of diffraction.

Bragg's law

$$n \cdot \lambda = 2 \cdot d \cdot \sin\theta$$

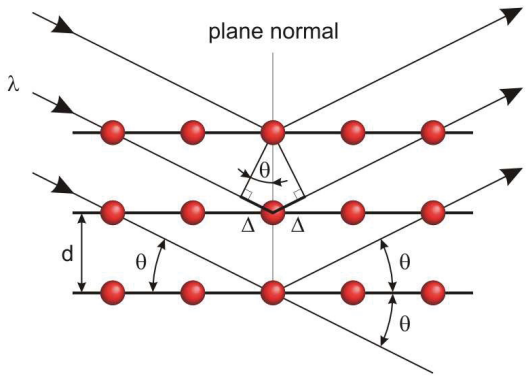

Fig 3.3 Bragg´s law [68] and the diffraction of incident X-ray waves at the atomic planes (modified [33]).

Within this work, a Panalytical X´Pert Pro was used for all samples investigated. The measurements have been carried out with glancing angle settings to gain surface near information and to diminish substrate peaks. The angle of incidence was set to 2°. The Panalytical X´Pert Pro was set up with a monochromatic Cu K_α radiation (λ=1.54056 Å) for the diffraction research.

Diffraction intensities are plotted versus 2θ angles, resulting in XRD patterns. The 2θ angle gives information about orientation and lattice spacing (d-spacing). This information can be used to evaluate the fractions of the different phases within a material, while tabulated 2θ values of reference materials have been compared to identify the phases formed. The tabulated values are provided by the Joint Committee on Powder Diffraction Standards (JCPDS).

3.2.6 Nanoindentation testing and evaluation

The investigation of hardness has been carried out with an ultra micro indentation system (UMIS) (Fig. 3.7). Within thin film hardness evaluation, an indentation depth of less than 10 % of the coating thickness is required to avoid substrate influences on the results [69]. Due to its precise mode of operation and therefore the achieved low indentation depths, the nanoindentation measurement is state of the art for thin film hardness characterization.

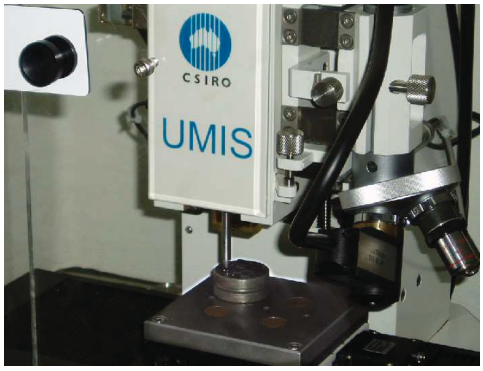

Fig. 3.7 Ultra micro indentationsystem.

The nanoindenter records load and displacement values while the diamond tip (here a Berkovich indenter, 3 sided pyramidal) is gently “pressed” into the materials surface (Fig. 3.8a.). This is called depth sensing indentation or instrumented indentation testing [33]. Force and depth are recorded for loading and unloading phases, and thus a load - displacement curve is plotted (Fig. 3.8 b). Generally, an elastic-plastic loading and an elastic unloading is observed [69]. The technique is standardized within DIN EN 14577, part 1-3 [70-72]. Typical

forces are on the mN scale and indentation depths are just a few hundred nm. Several indents are made to secure statistical representative hardness values.

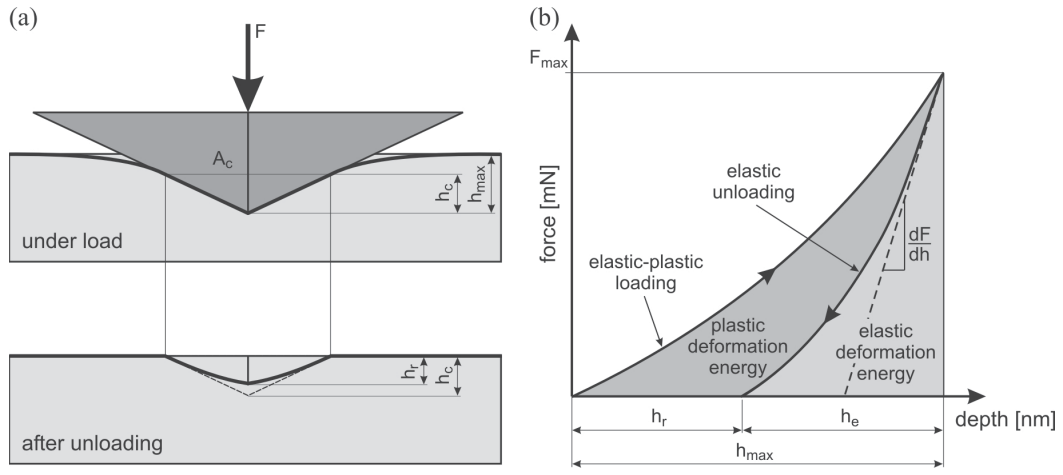

Fig. 3.8 a) Indent of a pyramidal indenter, applied with load F and the elastic-plastic behaviour illustrated through elastic shares (e.g. h_c-h_r). b) corresponding load displacement curve, h_e indicates the elastic shares of the maximum displacement value [33].

The evaluation of the load-displacement curves has been carried out with the Oliver-Pharr method [69]. As far as the hardness is the result of applied load divided by the projected contact area, the calculation of the indents real shape is of main importance. Therefore the IBIS software considers the present geometry of the indenters tip shape through calculation of the so called area function. Figure 3.9 illustrates the real geometry of the indenters tip and that there is a deviation from the perfect tip.

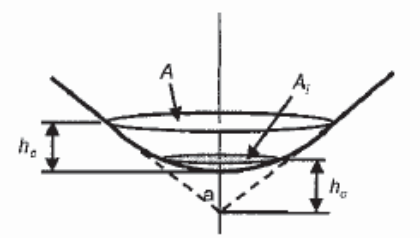

Fig. 3.9 Ideal tip versus (rounded) real tip geometry [69].

The precise contact depth is obtained through calculation of a geometry dependent factor and the contact stiffness (dF/dh) at h_{max}. Concerning the load – displacement curve, the upper 80 % of the unloading curve have been fitted to gain proper stiffness evaluation. Especially within thin film investigations, with little indentation depths, the area correction is of main importance, thus it is reported to have the greatest effect on accuracy of the final results [69].

3.2.7 Tribology

3.2.7.1 Tribological testing

Tribological testing has been implemented to find out in detail, which wear behaviour can be expected from the investigated coatings. Therefore a so called *ball on disc* experimental setup has been chosen. Tests were performed at room temperature and 700 °C to simulate high working temperatures. Within the "tribo test", an Al_2O_3 ball is clamped on the tip of a weight loaded metal tube, to scratch over a rotating disc of coated material. Thereby the ball is static and the sample rotates. Figure 3.5 shows a detailed overview of the CSM Instruments High Temperature Tribometer apparatus layout.

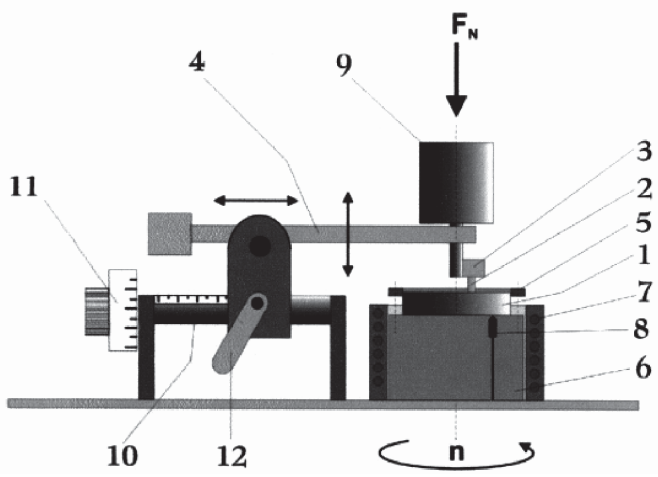

Fig. 3.5 CSM Tribometer 1) sample, 2) pin with ball on bottom tip, 3) pin holder, 4) lever, 5) locking ring, 6) rotation cylinder, 7) resistance heating, 8) thermocouple, 9) load, 10) radius adjustment axis, 11) radius adjusting screw, 12) lock for the lever arm [73].

This facility was also in use as a room temperature variant without heating and cooling device, but generally the same apparatus.

Defined testing conditions have been the same for all executed tests. The wear track radius has been set to 7 mm, the load was 5 N, the rotation speed was at 10 cm/sec and the sliding distance was 300 m, as previous experience showed these parameters to be best for valuable results. Tribometrical tests deliver friction coefficients and wear tracks to be analyzed.

3.2.7.2 Evaluation of tribological testing

To gain proper results concerning wear behaviour of the thin films deposited, the worn volume has been measured with optical methods. A so called optical profilometer was used to characterize the three dimensional surface structure of the worn sample. This apparatus works with the principle of a "Michelson-Interferometer". The Veeco Wyco NT 1000 (Fig. 3.6) splits the light beam into a reference beam and one that reflects on the samples surface. The reference beam reflects at the reference mirror. This alignment provides interference fringes when the two beams are merged, while best contrast is reached at best focus. Consequently, this interference pattern is measured with a camera and further calculations for the output of 3D and 2D illustrations are done by the Wyco software. Further calculations deliver results of the worn volume in positive and negative shares. As far as this method can not scan the entire wear track, five measurements have been carried out for each sample and then averaged to get representative values of the worn volume. After that procedure, the wear coefficient has been calculated.

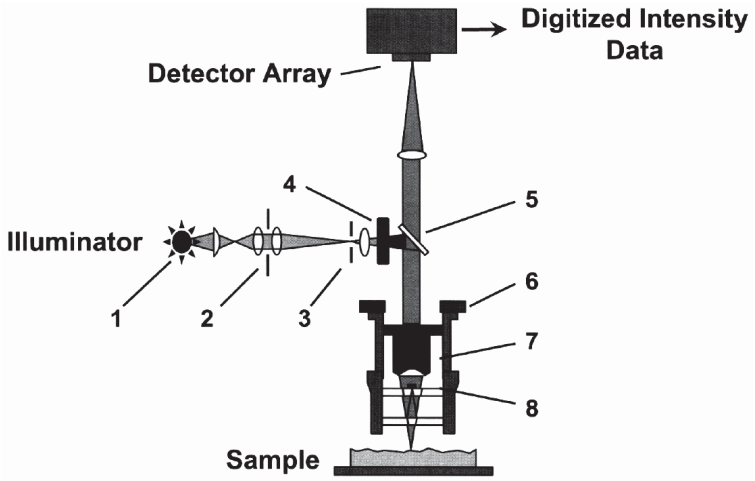

Fig. 3.6 Path of the light beam within the profilometer, 1) light source, 2) aperture stop, 3) field stop, 4) filter, 5) beam splitter, 6) translator, 7) microscope objective, 8) Mirau interferometer [74].

4 Results and discussion

4.1 X-ray diffraction

The analyses of the thin films phase morphologies by X-ray diffraction measurements have been of major interest within this work. Determining structure and the occurring phases of the single layer and the multi-layer TiAlN coatings provided information on the influence of bias voltage and alloying elements.
The following XRD patterns deal with information on phase composition of the single layered coatings, which have been combined to multi-layer versions. To provide a better comparability, both single and the respective combined multi-layer are displayed in the following figures on top of each other. Furthermore, the influence of bias voltage is displayed as a comparison of -40 V and -80 V XRD patterns. Beside the morphological cognitions on phase fractions, grain size can be compared through the peaks shape concerning sharpness and width. Thin and sharp peaks are often caused by bigger grains and broad peaks can be related to a smaller grain size [68]. Multi-layering can diminish the grain size in the main film growth direction through the alternating layers and the formation of new interfaces between these deposited materials [1].
The tabulated (JCPDS) peak positions are marked using coloured drop lines, representing the diffraction angles of fcc TiN (■), fcc AlN (□) and hcp AlN (⬢).
However, all peaks within the following plots show a deviation from the marked peak positions. The appearing peaks can be shifted either to smaller or higher diffraction angles compared to the drop lines.

4.1.1 TiAlN coatings

Figure 4.1 shows the XRD patterns of $Ti_{50}Al_{50}N$, $Ti_{33}Al_{67}N$ and the combination of both in a multi-layer structure ($Ti_{33}Al_{67}N/Ti_{50}Al_{50}N$) on top of the two single layer results. The -40 V bias coatings can be found in the left box and the -80 V ones in the right box. This structure will be kept for all of the following XRD patterns presented.
On the bottom of the left box in Fig. 4.1, the -40 V bias $Ti_{50}Al_{50}N$ single layer shows a single phase fcc structure and the related diffraction peaks at ~37.2°, ~43.5° and ~ 63°. Those peaks are located right in between of the fcc TiN and fcc AlN drop lines, due to the present solid solution (described in section 2.4). In comparison to that, the -40 V XRD plot of $Ti_{33}Al_{67}N$ in Fig. 4.1 shows fcc peaks at the same 2θ angles and additional hcp peaks at ~35°, ~48° and ~70°. These hcp phases are related to the higher Al content of this alloy (see also section 2.4). Peaks within this plot are broader and can thus be related to a smaller grain size.

The $Ti_{33}Al_{67}N/Ti_{50}Al_{50}N$ multi-layer (-40 V) shows well defined fcc peaks and diminished hcp peaks. The formation of this structure can be described with the so called *template effect*. This effect describes the structural evolution of a multi-layer coating, where ongoing growth is determined through the present phase on the surface. So, if there is already an fcc phase deposited on a substrate (e.g. $Ti_{50}Al_{50}N$), the following layer material tends to continue its growth with the present film's structure, even if its own usual structure would differ [75].
At the higher bias voltage of -80 V (Fig. 4.1, right box), a general observed effect is a peak shift to lower 2θ angles. This phenomenon can be related to the induced compressive stresses through higher energetic ions, widening the lattice spacing [35]. Another effect of increased bias voltage is a decrease of the Al content on the expense of hcp phase (more ionization of Ti atoms and backscattering of Al atoms). Dense structures are favoured through higher bias voltage and the grain size is reduced due to bombardment induced renucleation [38]. Furthermore, increased bias voltage decreases the fraction of hcp phases due to ion bombardment induced renucleation and so called collision cascade effects [38, 39]. The -80 V plots show these effects if compared to their -40 V versions, where for the $Ti_{50}Al_{50}N$ coating a decreasing grain size can be observed. The decrease of hcp peaks at ~35° and the grain size decrease can be seen for both, the $Ti_{33}Al_{67}N$ single and the multi-layer coating on top.

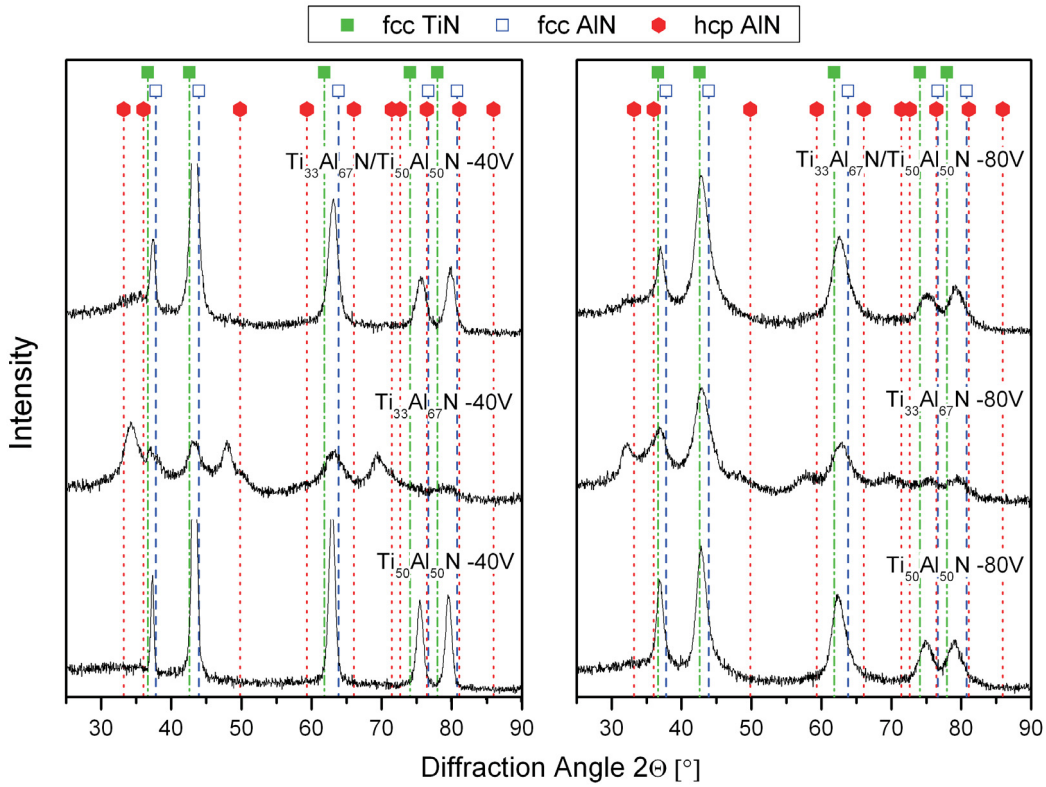

Fig. 4.1 XRD patterns of $Ti_{50}Al_{50}N$ and $Ti_{33}Al_{67}N$ single layer coatings compared to the $Ti_{33}Al_{67}N/Ti_{50}Al_{50}N$ multi-layer coatings. Left box -40 V, right box -80 V bias voltage.

Finally, it has to be mentioned that the $Ti_{33}Al_{67}N$ XRD patterns are in the following considered as a reference material for the investigated quarternary coating systems. Especially the hcp fraction is of interest, where the investigated single layer coatings show similar structures, induced by similar Al contents and low contents of alloying elements.

4.1.2 Ti-Al-B-N coatings

On the bottom of Figure 4.2, the reference $Ti_{50}Al_{50}N$ single layer coating (deposited at -40 V) can again be found showing the already described peak positions for the fcc solid solution structure with its characteristic sharp peaks. The -40 V B alloyed single layer XRD plot shows fcc peaks at similar positions and additional hcp peaks at ~34°, ~48° and ~69°. As reported by Kutschej et al., even small contents of B favour the formation of an additional hcp phase [76]. The Al content of the $Ti_{32.9}Al_{67}B_{0.1}N$ target is notably higher than within $Ti_{50}Al_{50}N$ and leads to higher hcp phase fractions. If compared to the $Ti_{33}Al_{67}N$ film in Fig. 4.1, the coating containing just 0.1 at % B shows an increased hcp phase content. According to Pfeiler et al., B is incorporated in both, the fcc and the hcp phases [77]. Finally, the multi-layer coatings XRD pattern (-40 V bias) shows a lower hcp peak at ~34° and much lower hcp peaks at ~48° and ~69°. All in all, the fcc peaks are much more distinct than the hcp phases and an answer thereon can be the template effect.
Increasing the bias voltage to -80 V provided the desired modifications within the materials. A main difference to -40 V bias is, that all peaks are shifted to smaller 2θ angles (wider lattice spacing) due to compressive stresses induced by the higher ion energies. The peaks are generally wider and less sharp, which is related to a smaller grain size as already mentioned. For the B alloyed single layer coating ($Ti_{32.9}Al_{67}B_{0.1}N$), the hcp peaks are significantly reduced by the higher bias voltage and the ~42.5° fcc peak increases compared to the coating grown at -40 V bias voltage. For the $Ti_{32.9}Al_{67}B_{0.1}N/Ti_{50}Al_{50}N$ multi-layer coating system, a decrease of hcp phase can be seen to be of major importance within the mentioned effects.

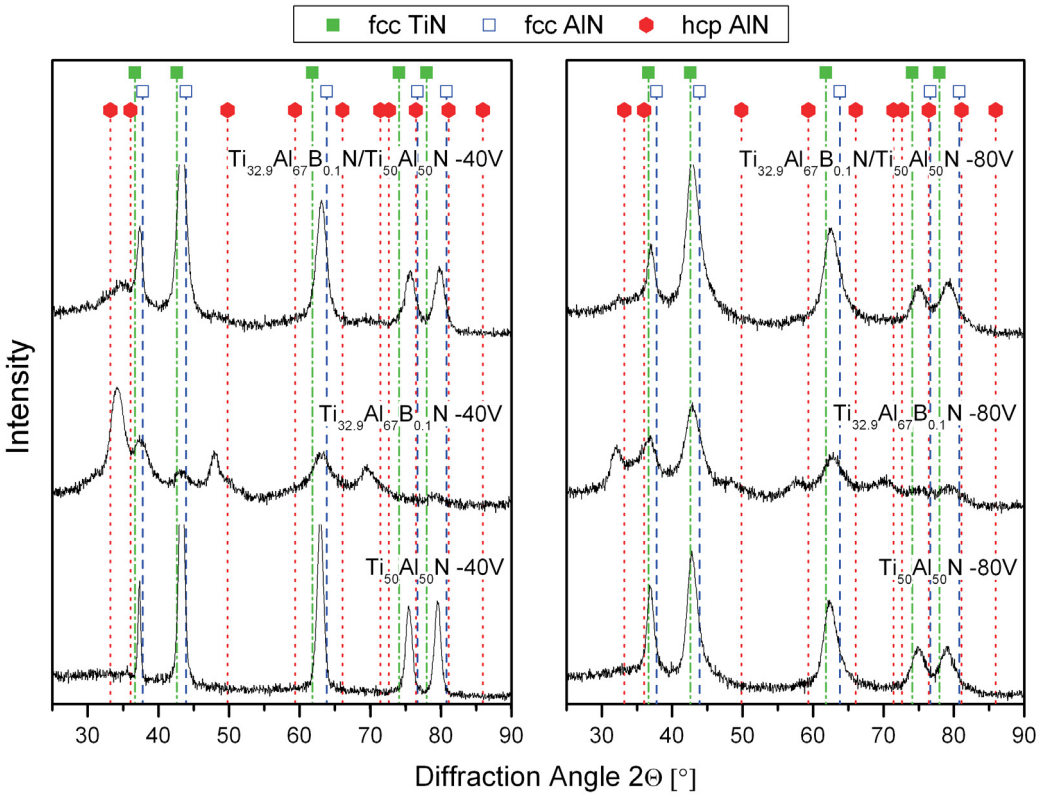

Fig. 4.2 XRD patterns of $Ti_{50}Al_{50}N$ and $Ti_{32.9}Al_{67}B_{0.1}N$ single layer coatings compared to the $Ti_{32.9}Al_{67}B_{0.1}N/Ti_{50}Al_{50}N$ multi-layer coatings. Left box -40 V, right box -80 V bias voltage.

4.1.3 Ti-Al-Ta-N coatings

Ta is known to foster the fcc structure in TiAlN systems on the expense of hcp phases [43, 59]. The left box in Fig. 4.3 illustrates the diffraction patterns of the Ta alloyed coatings deposited at -40 V bias voltage. The $Ti_{50}Al_{50}N$ peaks remain the same as already displayed earlier. $Ti_{31.7}Al_{63.3}Ta_5N$ shows three characteristic hcp peaks for -40 V at ~34°, ~47° and ~69°. The fcc peaks are found at angles of ~36.5°, ~43° and ~63°. Except from the very left and high hcp peak, the ratios between hcp and fcc peaks are low. In comparison to $Ti_{33}Al_{67}N$ in Fig. 4.1, the hcp phases are reduced by Ta alloying. The -40 V multi-layer design on top of Fig. 4.3 deals with almost sole fcc peaks caused by the already mentioned template effect. The biggest hcp peak of the Ta alloyed coating (~34°) strongly diminished and the other hcp peaks are not present within the multi-layer coating grown at -40 V bias voltage.

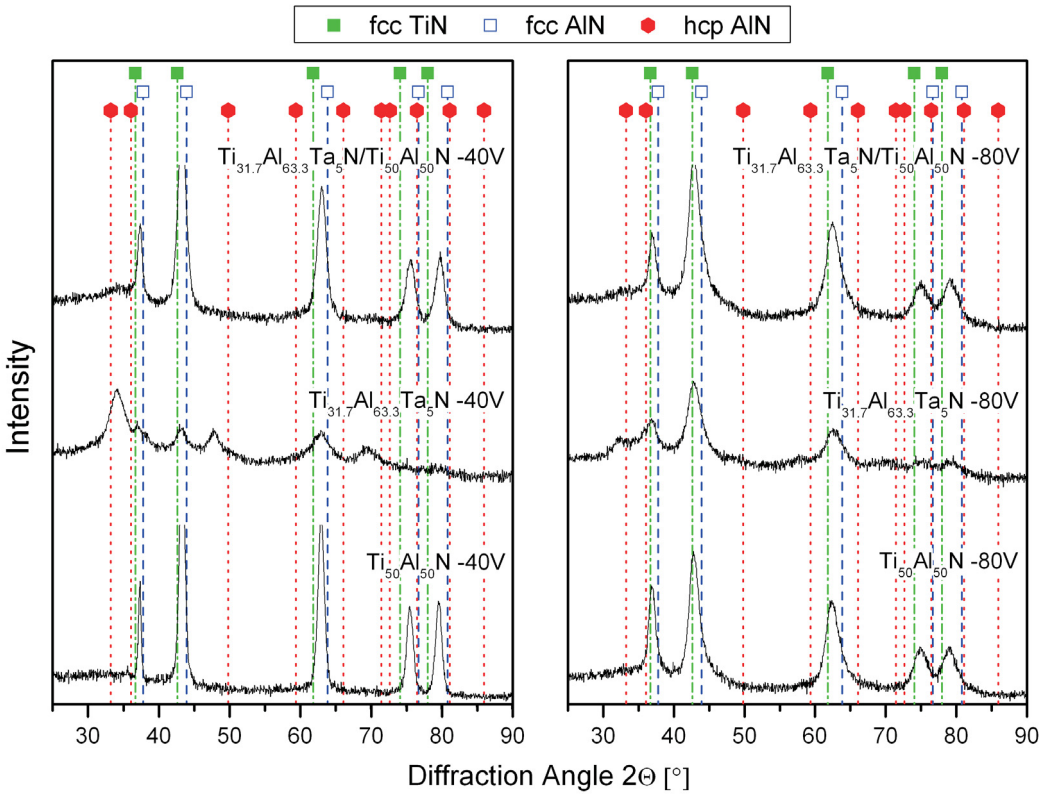

Fig. 4.3 XRD patterns of $Ti_{50}Al_{50}N$ and $Ti_{31.7}Al_{63.3}Ta_5N$ single layer coatings compared to the $Ti_{31.7}Al_{63.3}Ta_5N/Ti_{50}Al_{50}N$ multi-layer coatings. Left box -40 V, right box -80 V bias voltage.

For -80 V bias voltage (displayed in the right box of Fig. 4.3), the described peak shift to lower diffraction angles is observed for all peaks. The $Ti_{31.7}Al_{63.3}Ta_5N$ coating shows a strong change in phase composition due to the increased ion bombardment, where the hcp phases are almost disappearing. There are remaining traces of hcp phase, but if compared to -40 V, the fcc lattice is clearly favoured (see the small hcp peaks at ~32.5°, ~47°, ~69° and the increased fcc peaks at ~36°, ~42.5°, ~62.5°). Concerning the combination of the two films to a multi-layer coating, the trend of diminishing hcp phases (~32°) by the template effect can be determined. As mentioned before, the observed peak broadening is explained by smaller grain size, which can be related to biasing and multi-layering. Together with the hcp suppressing effect of the increased bias voltage, the formation of an almost sole single phase fcc structure can be seen.

4.1.4 Ti-Al-Si-N coatings

Si as an alloying element for TiAlN has shown to be favourable for the formation of hcp phases [78]. This is illustrated in Fig. 4.4 and especially for the -40 V bias conditions, the

effect shows up in form of a huge hcp peak on the very left end of the $Ti_{32.5}Al_{67}Si_{0.5}N$ single layer pattern (~34°). In contrast to that, the neighbouring fcc peak (~37°) remains small (compare Fig 4.1). The hcp peak at ~47° is intense in relation to the fcc peak next to it (~43°) and the fcc peak at ~63° is developed slightly better than the hcp peak at ~69°. The -40 V multi-layer on top shows again the already mentioned phenomenon of the template effect. Even the highly hcp phase supporting Si alloyed coating is forced to high fcc phase contents by multi-layering. There is a broad hcp peak remaining at ~34.5° and small ones at ~47° and ~69°, but the well defined fcc peaks are dominant.

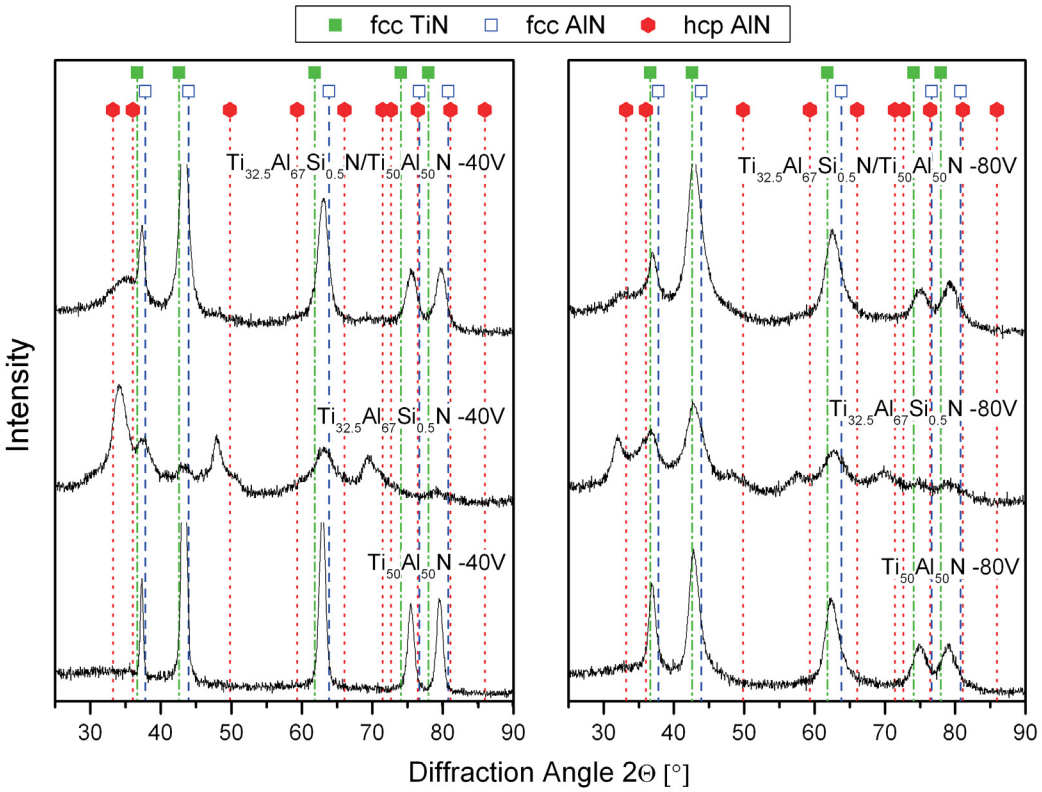

Fig. 4.4 XRD patterns of $Ti_{50}Al_{50}N$ and $Ti_{32.5}Al_{67}Si_{0.5}N$ single layer coatings compared to the $Ti_{32.5}Al_{67}Si_{0.5}N/Ti_{50}Al_{50}N$ multi-layer coatings. Left box -40 V, right box -80 V bias voltage.

Silicon alloyed coatings grown at higher bias voltages (-80 V) again show the named effect of peak shifting, as well as a decrease of hcp phase fractions. If the $Ti_{32.5}Al_{67}Si_{0.5}N$ -40 V pattern is compared to the -80 V pattern, a drastic change in phase ratios can be observed. The fcc phase content is increased on the expense of hcp fractions. All hcp peaks get widened, evidencing a smaller grain size. The multi-layer deposited at -80 V shows shifted and widened peaks as discussed and as a major difference to the lower bias voltage, the hcp phase also diminishes. In general, the Ti-Al-Si-N coatings are found to have similar phase ratios and peak shapes as the B containing coatings (compare Fig. 4.2).

4.1.5 Ti-Al-V-N coatings

V has been alloyed in two different compositions of 16.5 at. % and 25 at. % and its effects will be presented separately in the following two sections.

$Ti_{16.5}Al_{67}V_{16.5}N$ coatings

The $Ti_{16.5}Al_{67}V_{16.5}N$ single layer coating grown at -40 V bias voltage shows noteworthy fractions of hcp phase, illustrated by the ~35° peak in Fig. 4.5. This is caused by the remarkable Al content of 67 %. Kutschej et al. found the V within TiAlN to be responsible for fcc lattice enforcement [43]. This is expressed especially by the fcc peak at ~44°, but also the peaks at ~37.5° and ~64° are higher than their neighbouring hcp peaks at the diffraction angles of ~35°, ~48° and ~70° (see again Fig. 4.1). The V alloyed multi-layer coating shows a similar XRD pattern to the already discussed alloyed TiAlN coatings in this section. In case of V, a strong influence of the template effect and an almost sole fcc structure (except for a very small hcp peak at ~34.5°) is found.

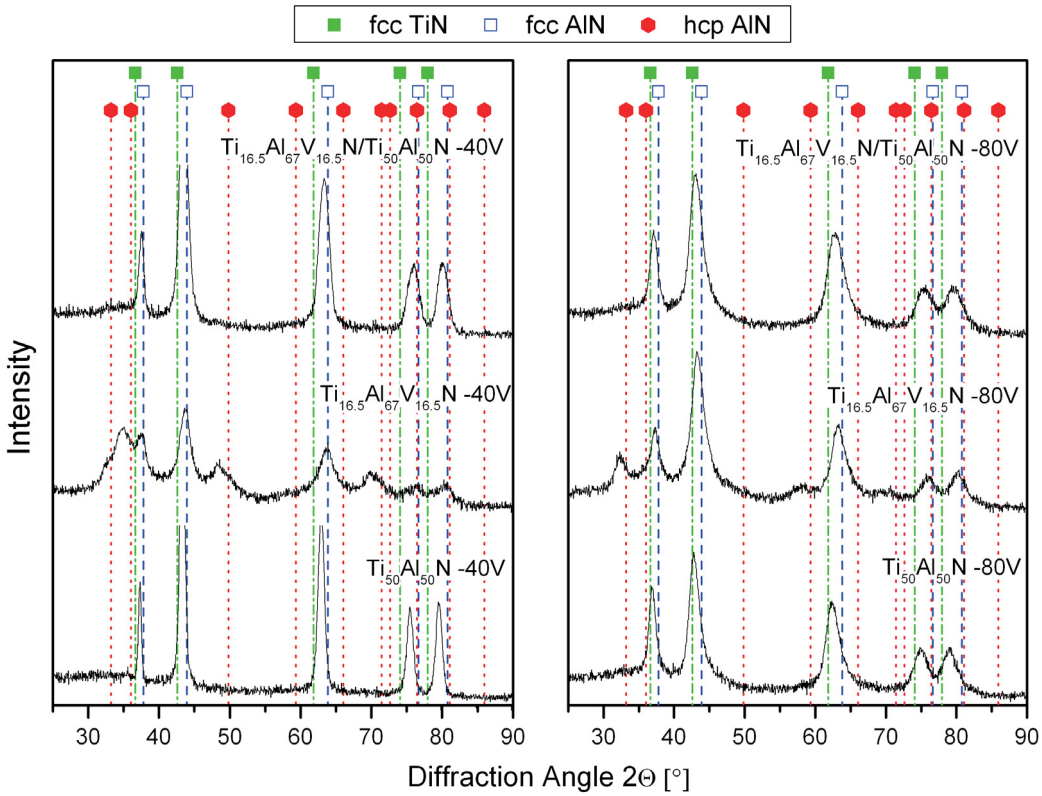

Fig. 4.5 XRD patterns of $Ti_{50}Al_{50}N$ and $Ti_{16.5}Al_{67}V_{16.5}N$ single layer coatings compared to the $Ti_{16.5}Al_{67}V_{16.5}N/Ti_{50}Al_{50}N$ multi-layer coatings. Left box -40 V, right box -80 V bias voltage.

Concerning the single layer coating alloyed with 16.5 at. % V, a change to more fcc phase fraction and a decreased grain size can be found for the coating system grown at higher applied bias voltage of -80 V (Fig. 4.5 right box). This correlates to the already mentioned effects of increased bias voltage on alloyed TiAlN coatings. Especially the fcc peak at ~43.5° gains in intensity. For the -80 V bias voltage multi-layer coating, the already mentioned phenomena of peak broadening, peak shifting and the gain of fcc phase fractions on the expense of hcp fractions (template effect), are illustrated in Fig 4.5.

$Ti_8Al_{67}V_{25}N$ coatings

The second V alloyed coating contains a higher amount of the element and its XRD patterns in Fig. 4.6 show the reported effect [43] of enhanced fcc phase formation, due to V alloying (compare the $Ti_{33}Al_{67}N$ and $Ti_{16.5}Al_{67}V_{16.5}N$ patterns in Fig. 4.1 and Fig. 4.5). Although the hcp peak at ~32.5° increased in comparison to the lower V content of the single layer coating in Fig. 4.5, the neighbouring hcp peak at ~35° and all other hcp peaks decreased. The fcc peaks are now dominant compared to the coating with a V content of 16.5 at. %.
The $Ti_8Al_{67}V_{25}N/Ti_{50}Al_{50}N$ multi-layer coating deposited at -40 V bias voltage shows no more hcp phases (compare Fig. 4.5), but well defined fcc peaks which again can be related to the template effect.

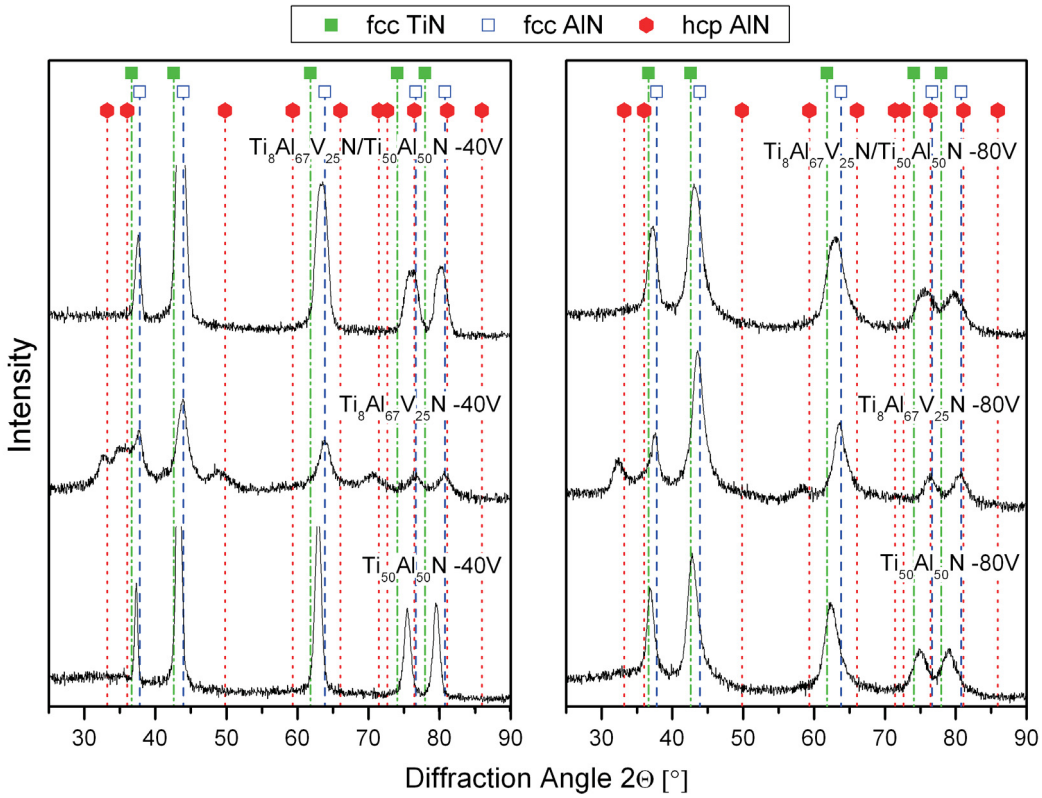

Fig. 4.6 XRD patterns of $Ti_{50}Al_{50}N$ and $Ti_8Al_{67}V_{25}N$ single layer coatings compared to the $Ti_8Al_{67}V_{25}N/Ti_{50}Al_{50}N$ multi-layer coatings. Left box -40 V, right box -80 V bias voltage.

Higher bias voltage (-80 V) results in hcp phase decrease and a remarkable increase of fcc phase as discussed (compare the single layer fcc peak at ~43.4° for -40 V and -80 V in Fig. 4.6). The effect of higher ion energy again leads to higher compressive stresses, wider lattice spacing and a resulting peak shift. Furthermore the grain size decreased. Finally, the multi-layer system deposited at -80 V bias voltage shows up entirely fcc structured and with smaller grains than the one deposited at -40 V. These results from the template effect and the influence of increased bias voltage concerning a grain size decrease and an fcc promoting nature.

4.2 Hardness and Young's modulus

Obviously the hardness of hard coatings for cutting tool applications is of major interest. Machining conditions and lifetime are often limited by hardness values. The Young´s modulus also plays a major role within this context and especially its regulation on demand is of interest.

Generally, all the investigated materials show an increase of hardness, if the bias voltage is increased from -40 V to -80 V. The higher bias voltage causes higher defect densities and higher stresses are induced [35]. One-dimensional defects as Frenkel defects and interstitial atoms cause effects similar to cold work hardening. Compressive stresses with higher bias voltages are also displayed in the XRD section, where the resulting peak shifts to lower diffraction angles have been discussed. Furthermore, all multi-layer designs show higher hardness values than the single layer versions. The template effect causes higher fcc phase contents, which results in higher hardness in comparison to the hcp phases. Bull et al. reported on the hardening within multi-layer coatings to be dependent on interfacial and surface energy effects [79]. Long et al. found the increase of hardness might not be significantly influenced by the multi-layers wavelength and concluded the higher hardness increases reported by others to be associated with high internal stresses. He also related this effect to be responsible for high hardness increases of single layer systems [80]. The formation of new interfaces between the deposited layers causes smaller grains [1], which favours a hardness increase according to the well known Hall Petch effect.
The Young´s modulus (YM) is known to be dependent on the crystalline orientation, as it is at a maximum in the closest packed direction of the lattice [81]. This is the reason why (concerning the closed packed direction) the YM within fcc lattices is higher than the one of hcp structured lattices. The YM also depends on the grain size, because a smaller grain is accompanied by the formation of additional interfaces, because the less crystalline fractions at the grain boundaries increase and thus the YM decreases.

4.2.1 TiAlN coatings

First of all the unalloyed $Ti_{33}Al_{67}N$ single layer and the $Ti_{33}Al_{67}N/Ti_{50}Al_{50}N$ multi-layer coating are shown in Fig. 4.7 to display their behaviour concerning hardness and YM, at varied bias voltages. The $Ti_{33}Al_{67}N/Ti_{50}Al_{50}N$ multi-layer coating shows significantly higher hardness values for both bias voltages compared to the single layer films. This can be related to the fact that the template effect promotes the formation of fcc phases. If these graphs are related to the structure analysis in the XRD section (Fig. 4.1), it can be seen that the multi-

layer coating shows smaller grains at increased bias voltage. This grain refinement hardens the material (Hall Petch effect). Hardness is also influenced positively by the high fcc phase content. Bias voltage itself induces more stresses and defects [38], which also increases the hardness of the material. In case of the single layer coating, the YM increases with higher bias voltage, which can be related to the increase of fcc lattice fractions. As far as the multi-layer coatings' phase composition do not change radically with the bias voltage increase (see Fig. 4.1), the decreasing YM for higher bias voltage (Fig. 4.7) can be related to the smaller grain size and the corresponding increase of interfaces.

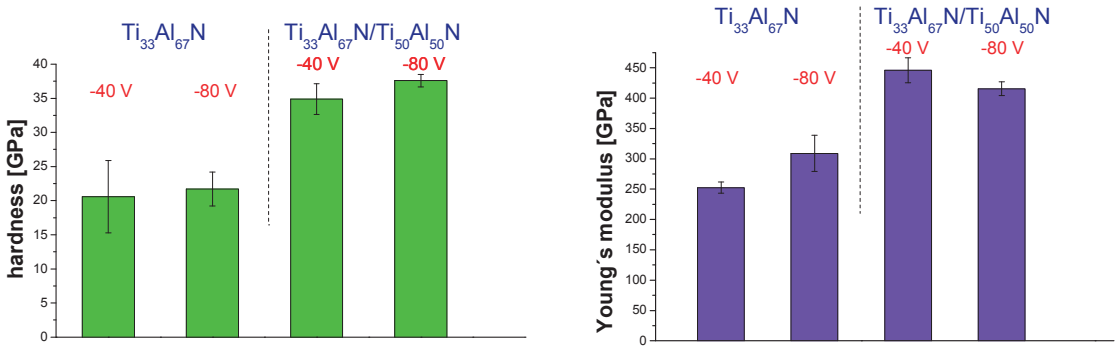

Fig. 4.7 Increase of hardness and YM of the $Ti_{33}Al_{67}N$ single layer coating for -40 V and -80 V bias voltage.

4.2.2 Ti-Al-B-N coatings

The hardness and YM values of B alloyed TiAlN single and multi-layer coatings and those for the $Ti_{50}Al_{50}N$ template layer (all for -40 V and -80 V bias) are shown in Fig. 4.8.
Related to the investigated structures of these coatings (see XRD patterns in Fig. 4.2), $Ti_{32.9}Al_{67}B_{0.1}N$ shows the effect of increasing fcc fractions with higher bias voltage and thus hardness rises, the YM increases as well, which is related to the effect of high fcc phase contents. Since the $Ti_{50}Al_{50}N$ template material shows a single phase fcc structure already at -40 V bias, the hardening at -80 V bias might be explained by grain refinement, which correlates with the decreasing YM (induced by an increasing amount of less crystalline regions). Increasing compressive stresses would increase hardness and YM, which suggests grain refinement as the dominant effect. The multi-layer coating system shows maximum hardness, since the template effect promotes the fcc phase. Higher bias voltage (-80 V) also increases the fcc fractions of the multi-layer system, which leads to an additional hardness increase. The YM of the multi-layer coating grown at -80 V bias voltage drops compared to

the one grown at -40 V. This can be related to the smaller grain size at higher bias voltage, which has been observed in the XRD results (see Fig. 4.2).

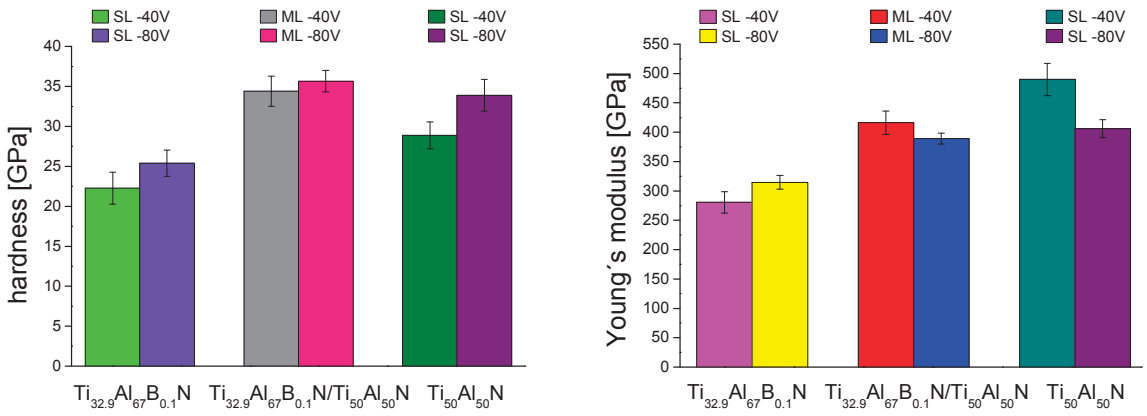

Fig. 4.8 Hardness and YM of the B alloyed single layer (SL) and multi-layer (ML) coatings and the template material single layer coating, all at -40 V and -80 V bias voltage.

4.2.3 Ti-Al-Ta-N coatings

The hardness graph in Fig. 4.9 shows the same general relation concerning hardness increase with the bias voltage increase as already discussed. Ta is known to promote the fcc phase [39, 59, 82], which should result in increased hardness. However, a comparison of TiAlN (Fig. 4.7) and the quarternary Ta alloyed coating (both -40 V bias voltage) shows no significant hardness improvement. The coatings grown at higher bias voltage of -80 V have a higher amount of lattice defects and fcc phase fraction and thus the hardness of these coatings increases. The same is valid for the YM. Compared to the Ti-Al-B-N coatings in Fig. 4.8, the hardness and the YM increase are significantly higher for the Ta alloyed coatings, which might be caused by the fcc promoting effect of Ta. The $Ti_{50}Al_{50}N/Ti_{31.7}Al_{63.3}Ta_5N$ multi-layer coating shows high hardness (34.8 GPa) and a pronounced increase with higher bias voltage (36.7 GPa). The almost sole fcc phase structure is expected to result in an increased YM, but a decreasing YM has been observed and can be related to smaller grains as discussed (more interfaces).

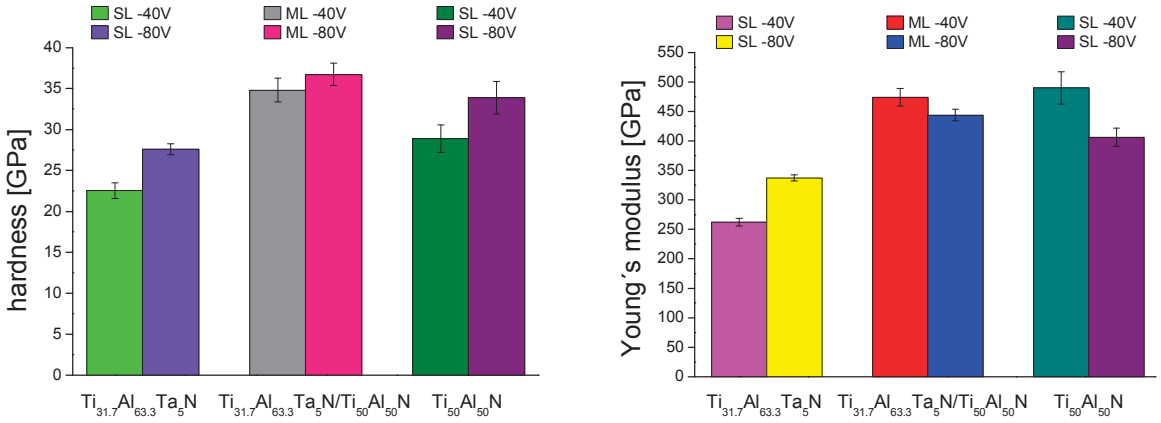

Fig. 4.9 Hardness and YM of the Ta alloyed single (SL) and multi-layer (ML) coatings and the template material single layer coating, all at -40 V and -80 V bias voltage.

4.2.4 Ti-Al-Si-N coatings

Durand-Drouhin et al. report on the hardening influence of Si alloyed to TiAlN and that the YM is not notably influenced thereby. They mention the Hall Petch effect to be responsible for their observations [55]. Derflinger et al. also found the Hall Petch effect to influence the hardness positively and additionally report on distortion of the lattice through the smaller Si atoms (compared to Al) and an increase in hardness, respectively [67].

Since as Si is known to promote hcp phases [78] and in fact the Si alloyed TiAlN is two phased, one would expect lower hardness and YM values for the $Ti_{32.5}Al_{67}Si_{0.5}N$ coatings compared to the fcc $Ti_{50}Al_{50}N$ coatings. Concerning the single layer coating, hardness and YM do show this expected behaviour (Fig. 4.10), with the lowest values of all investigated coating systems at -40 V and -80 V bias voltage. Compared to the XRD pattern in Fig. 4.4, the hcp fraction of the $Ti_{32.5}Al_{67}Si_{0.5}N$ coating decreases with higher bias voltage, but still remains higher than for all the other single layer coatings investigated within this work. The observed YM increase with higher bias voltage can be related to the decreasing hcp phase. Although hardness is significantly increased for the $Ti_{32.5}Al_{67}Si_{0.5}N/Ti_{50}Al_{50}N$ multi-layer coating, the hardness level remains the lowest of the competing multi-layer coating systems in this work. However, a remarkable increase of hardness is provided by the increase of bias voltage. Concerning the multi-layer coatings' YM, a slight increase is taking place with increasing bias voltage, which suggests the decreasing hcp fraction (caused by the template effect) to be the dominant factor and not the decreasing grain size, which would have caused lower YM values. This tends to be induced by the almost sole fcc structure (see Fig. 4.4),

reached by multi-layering and the higher bias voltage, while the template effect seems to be predominant.

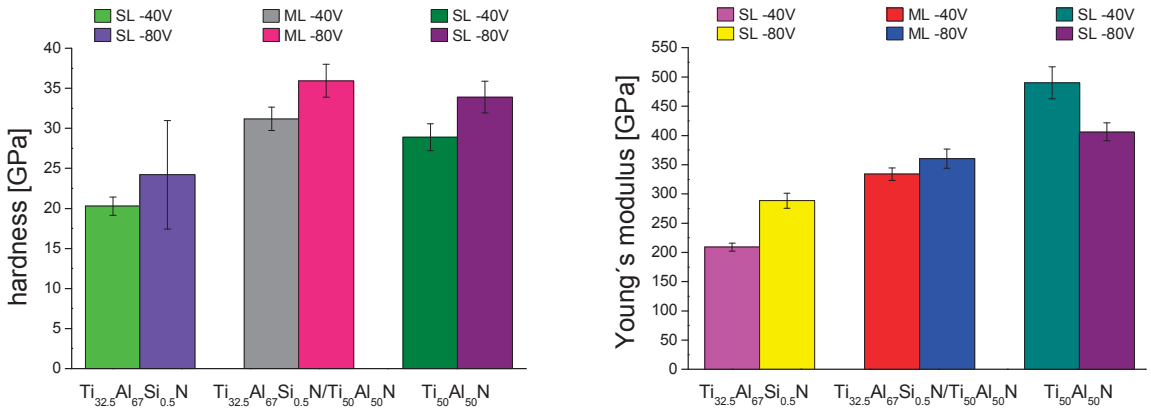

Fig. 4.10 Hardness and YM of the Si alloyed single (SL) and multi-layer (ML) coatings and the template material single layer coating, all at -40 V and -80 V bias voltage.

4.2.5 Ti-Al-V-N coatings

Vanadium alloying of TiAlN coatings has been described to promote the fcc structure within this system [39]. This is also reflected within the present work. An increased hardness value can be found for the $Ti_{16.5}Al_{67}V_{16.5}N$ single layer coating grown at -40 V bias voltage (Fig. 4.11), if it is compared to the single layer reference coating $Ti_{33}Al_{67}N$ (-40 V) in Fig. 4.7. Furthermore, the related XRD patterns in Fig. 4.1 and Fig. 4.5 show the structural differences and especially the higher fcc phase content of the V alloyed TiAlN coating. Concerning an increase of bias voltage, this coating system shows also the described fcc phase enhancement and so the hardness values increase from ~27.6 GPA (-40 V) to ~34.3 GPa (-80 V). In case of the $Ti_{16.5}Al_{67}V_{16.5}N$ single layer film, also the YM increases with higher bias voltage, which can be related to the higher fcc phase content of coatings grown at -80 V bias voltage.
For the V alloyed multi-layer coatings with a V content of 16.5 at. % (Fig. 4.11), hardening is provided by the described template effect (fcc phase increase) and the reduced grain size (Hall Petch effect). The introduction of higher bias voltage induces higher compressive stresses and smaller grains within dense structures. As a consequence, higher hardness values are reached for the -80 V multi-layer coating. Contrary to that, the YM value decreases remarkably with the higher bias voltage, which can be related to grain size effects already described (higher amounts of interfaces let the YM decrease).

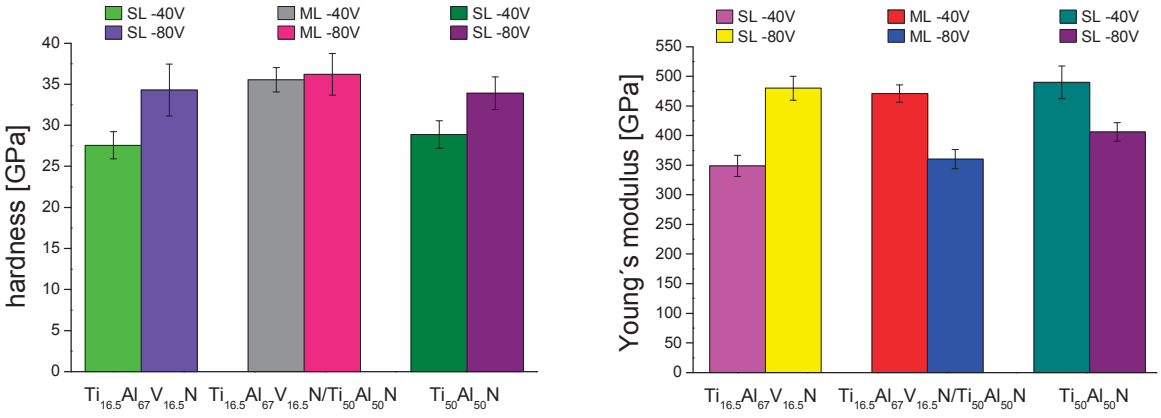

Fig. 4.11 Hardness and YM of the 16.5 at. % V alloyed single (SL) and multi-layer (ML) coatings and the template material single layer coating, all at -40 V and -80 V bias voltage.

For higher V contents (25 at. % V), as displayed in Fig. 4.12, the single layer coating grown at -40 V bias voltage shows lower hardness as the -80 V version. This can be related to higher fcc phase contents and the grain size decrease with higher bias voltage (compare the XRD pattern in Fig. 4.6), while in this case the promotion of the fcc phase seems to be the dominant effect.

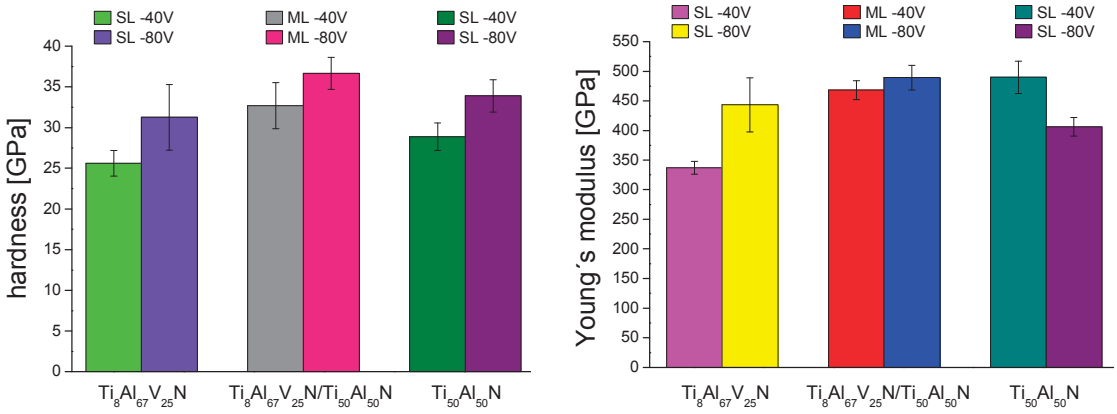

Fig. 4.12 Hardness and YM of the 25 at. % V alloyed single (SL) and multi-layer (ML) coatings and the template material single layer coating, all at -40 V and -80 V bias voltage.

The multi-layer coating also shows the discussed behaviour of hardness increase with higher bias voltage. Here, the grain refinement induced by the higher bias voltage seems to be the main effect that can be named responsible for the higher hardness (Hall Petch effect).

Concerning the YM, the single layer coatings behave as already discussed for the $Ti_{16.5}Al_{67}V_{16.5}N$ single layer coatings and show an increased fraction of fcc phase. The XRD patterns for both V alloyed multi-layer coatings (16.5 at. % and 25 at. % of V) in section 4.1 show similarities, but the YM of the 25 at. % V containing multi-layer coating shows a different behaviour. Although the grain size decreases for the -80 V multi-layer coating (higher fractions of amorphous regions), the YM increases in relation to the -40 V multi-layer coating. Obviously, another effect should be taken into account, which is not jet clear and so further investigations are needed to clarify this point.

4.3 Oxidation resistance

Concerning the improved oxidation behaviour of TiAlN coatings in comparison to TiN coatings, further improvements have been reached through adjustments of the Al content. PalDey et al. report on the increase of oxidation initiation temperatures for TiAlN coatings with elevated Al contents (60-70 % Al) up to 950 °C [1]. For Al contents of 50 %, they reported 700 °C as oxidation temperature (see Fig. 2.17). Several authors found the Al_2O_3 layer on TiAlN coatings to provide higher oxidation resistance, than the Ti- based oxides on TiN coatings do [32, 83]. Alloying of a fourth element and the introduction of quarternary coating systems is a further approach to increase the oxidation behaviour.
The present work concentrates on the observation of oxide layer formation after annealing tests at 900 °C for 60 min for B, Ta and Si alloyed single and multi-layer coatings. Due to their lower oxidation resistance, the V alloys (single and multi-layers) were annealed at 650 °C for 30 min. Kutschej et al. reported on Ti-Al-V-N coatings with 10 and 25 at. % V, to show a stable structure up to 500 °C and found new phases of V oxides at 700 °C [43].
SEM images of fracture cross sections have been chosen to illustrate the oxide layer thickness of the investigated coating systems. Again two different bias voltages (-40 V and -80 V) have been studied; however, the majority of the -80 V samples did not survive the annealing process, which means that either the film or the whole sample disrupted during the test.

4.3.1 Ti-Al-X-N coatings (X= B, Si, Ta)

Figure 4.13 illustrates the fracture cross sections of annealed Si and Ta multi-layer samples. These SEM images show almost the same result, where an oxide layer is formed on top of the nitride, which protects the coating beneath. The oxide layer thickness can be related to the oxidation resistance, where the Si alloyed multi-layer (Fig. 4.13 a) shows a thinner oxide layer (~190 nm) than the Ta alloyed multi-layer coating (~380 nm) in Fig. 4.13 b).

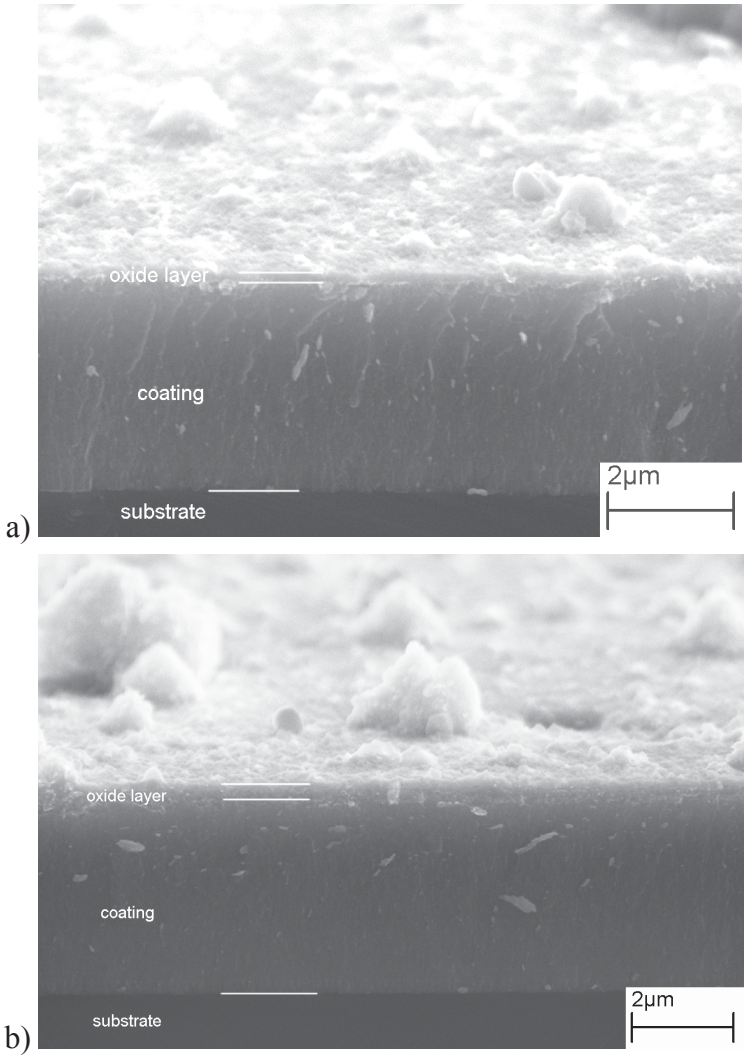

Fig. 4.13 SEM images of fracture cross sections after annealing (900 °C; 60 min), a) Ti-Al-Si-N/$Ti_{50}Al_{50}N$ multi-layer coating. b) Ti-Al-Ta-N/$Ti_{50}Al_{50}N$ multi-layer coating. Both grown at -40 V bias voltage.

The oxide layer thickness on the Ti-Al-Si-N/$Ti_{50}Al_{50}N$ multi-layer is significantly lower, than for its individual single layers (Fig. 4.14). There, $Ti_{50}Al_{50}N$ shows low oxidation resistance and the Ti-Al-Si-N has a significantly higher oxidation resistance. TiAlN films are known to form protective Ti and Al oxide layers, due to the segregation of Ti and Al atoms at high temperatures [67]. For Si alloyed films, Tanaka et al. claimed an Al-Si-oxide on top of the coating to provide enhanced oxidation barrier effects compared to unalloyed TiAlN films [84]. Vaz et al. reported that Si within TiAlN leads to the formation of hcp phases and that hcp phases do have a destructive influence on the oxidation resistance of alloyed TiAlN films. They also noted a positive effect on the oxidation resistance by a higher Al content up to a critical concentration and a negative effect beyond this critical concentration (where hcp phases are formed) [78]. Contrary to that, Pfeiler et al. reported on improved oxidation resistance of Si or B doped coatings, which is related to a modified oxidation sequence [77].

If these two discussed single layer coatings are combined to a multi-layer system, the oxidation resistance is enhanced and this can be related to the promoted formation of fcc structure by multi-layering (template effect), which combines the positive effects of Si doping and a single phase fcc structure.

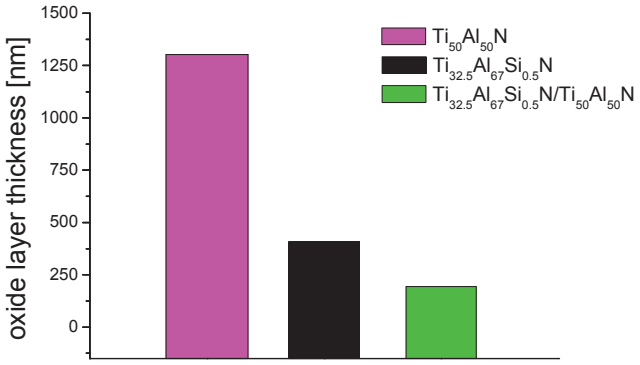

Fig. 4.14 Oxide layer thicknesses after annealing (900 °C; 60 min). Individual single layer coatings and their combination as a Si alloyed multi-layer coating (-40 V bias).

Pfeiler et al. reported on the increase of oxidation resistance, due to Ta alloying of TiAlN coatings [59], which was also confirmed in the present work. The oxide layer thicknesses of the $Ti_{50}Al_{50}N$ and the Ta alloyed single layer coatings are compared in Fig. 4.15, where the beneficial effect on oxidation resistance by Ta alloying can be confirmed.
The oxide layer thickness of the Ta alloyed multi-layer coating (Fig. 4.15) increases in relation to its single layer version. Concerning this observation, it can be concluded that the multi-layer design does not positively affect the oxidation behaviour of the Ta alloyed coating. This could be explained by the higher initial fcc phase content of the Ta alloyed single layer coating and thus the improvement by the template effect is smaller as seen for the Si doped coating in Fig. 4.14. The main negative effect on the oxidation resistance of the Ta alloyed multi-layer coating can be found in the lower Ta content of the multi-layer coating system, if this is compared to the Ti-Al-Ta-N single layer version.

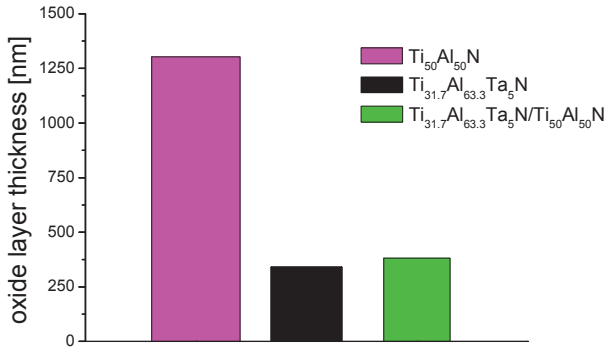

Fig. 4.15 Oxide layer thicknesses after annealing (900 °C; 60 min). Individual single layer coatings and their combination as a Ta alloyed multi-layer coating (-40 V bias).

Finally Fig. 4.16 gives an overview of the oxide layer thicknesses of the Si- and Ta containing coatings grown at -40 V bias voltage and illustrates the advantage of alloying compared to the ternary TiAlN reference material. Further it can be seen that different effects are dominant for the Si and the Ta alloyed coatings. In case of Si as an alloying element, both alloying and multi-layering results in enhanced oxidation resistance. For Ta alloyed coatings with their higher fcc phase containing structure, the content of the alloying element is of major importance for the oxidation resistance and thus the multi-layers oxidation resistance is slightly lower. This is caused by the lower amount of Ta inside the multi-layer coating compared to the single layer coating.

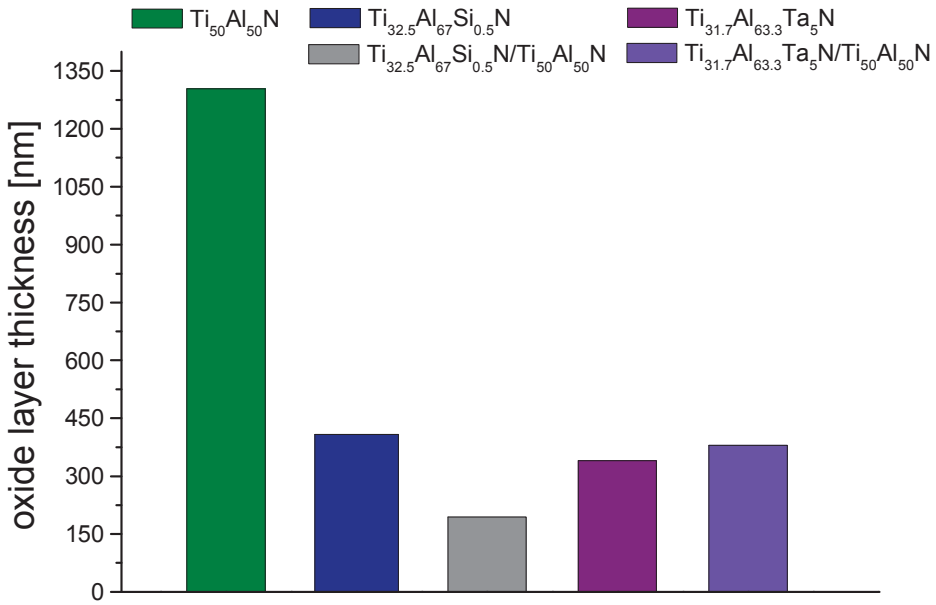

Fig. 4.16 Overview of oxide layer thicknesses of annealed (900 °C; 60 min) Si- and Ta alloyed coatings grown at -40 V bias voltage.

The B alloyed multi-layer sample (-40 V bias) did not survive the annealing procedure. All the film material has been gone and just fractures of substrate material remained.
However, previous investigations [85] and [77] showed improved oxidation behaviour of B doped TiAlN and a comparable behaviour of Si doped coatings. Thus it is suspected that the behaviour of B containing multi-layers could be similar to Si alloyed multi-layer coatings.

4.3.2 Ti-Al-V-N coatings

SEM cross sections of oxidized Ti-Al-V-N coatings with a content of 16.5 at. % V, grown at -40 V bias voltage, are illustrated in Fig. 4.17. The single layer film system in Fig. 4.17 a) shows a distinct oxide layer on top, while the multi-layer system in Fig. 4.17 b) does not show any oxide formation. The annealed multi-layer sample shows the characteristic grey colour of an as deposited Ti-Al-V-N coating, which suggests that the sample was not or nearly not oxidized. This can be related to the hindered out-diffusion of V by the $Ti_{50}Al_{50}N$ template layers and therefore also less in-diffusion of O_2 takes place. Both is known to be responsible for the relatively high oxidation rate of V alloyed single layer coatings [43, 86].

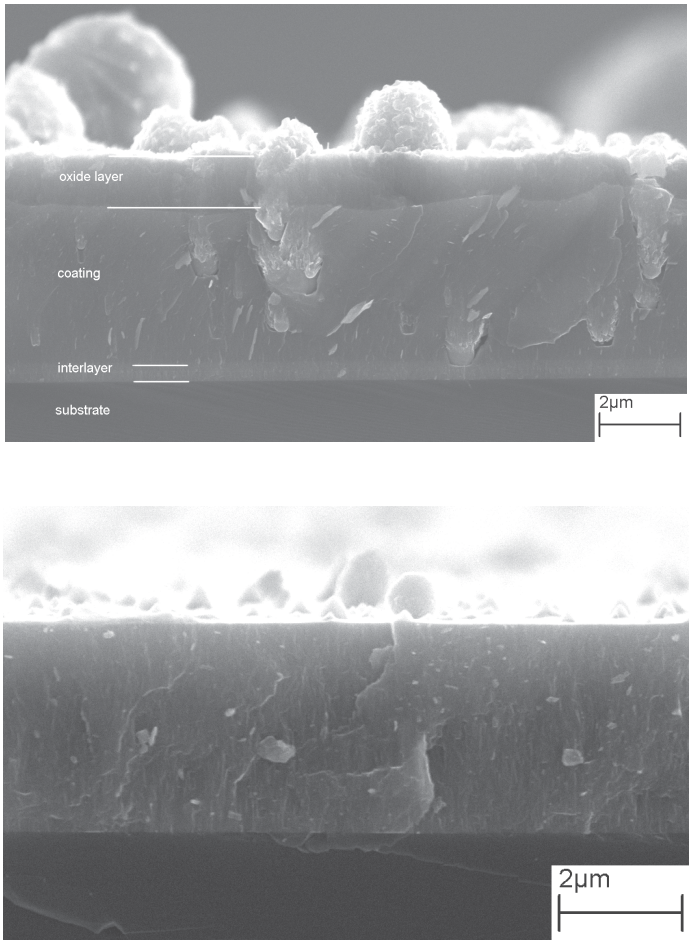

Fig. 4.17 SEM fracture cross section images of annealed (650 °C; 30 min) a) $Ti_{16.5}Al_{67}V_{16.5}N$ single layer coating, b) $Ti_{16.5}Al_{67}V_{16.5}N/Ti_{50}Al_{50}N$ multi-layer coating. Both grown at -40 V bias voltage.

For higher V contents of 25 at. % V, the oxidation behaviour changes as described earlier. Kutschej et al. reported on the higher oxidation rate with increasing V contents and higher temperatures [43]. Fig. 4.18 a) displays the annealed $Ti_8Al_{67}V_{25}N$ single layer coating and its massive oxide layer of 3500 nm thickness. In comparison to that, its multi-layer version shows no significant oxide formation that could be measured (Fig. 4.18 b).

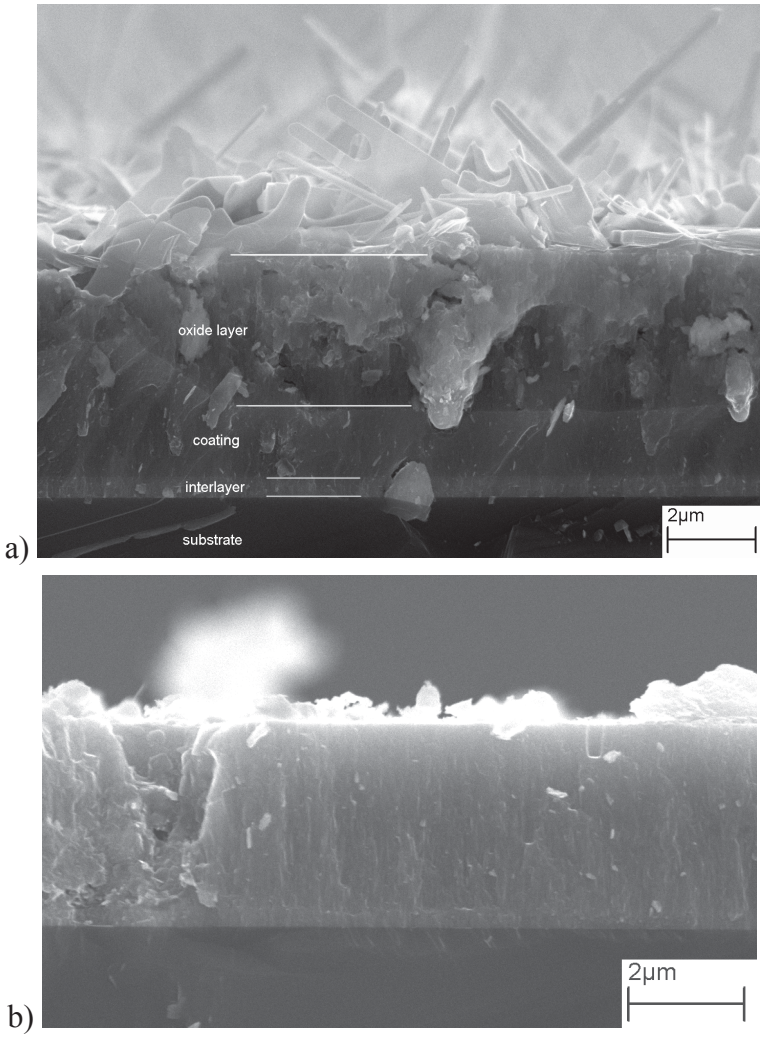

Fig. 4.18 a) SEM fracture cross section images of annealed (650 °C; 30 min) a.) $Ti_8Al_{67}V_{25}N$ single layer coating, b) $Ti_{50}Al_{50}N/Ti_8Al_{67}V_{25}N$ multi-layer coating. Both grown at -40 V bias voltage.

If the surface of the $Ti_{50}Al_{50}N/Ti_8Al_{67}V_{25}N$ multi-layer coating is visually characterized, a slight change in colour from grey (as deposited) to blue has been observed which indicates starting oxidation. If this is related to the multi-layer coating that contains only 16.5 at. % V, a higher oxidation rate is found for the higher V content of 25 at. %. It can thus be concluded that higher V contents lead to higher oxidation rates (more diffusion paths) and multi-layering leads to lower oxidation rates ($Ti_{50}Al_{50}N$ layers act as diffusion barriers).
To provide a better overview, the oxide layer thicknesses of the samples grown at -40 V bias voltage are displayed in Fig. 4.19.

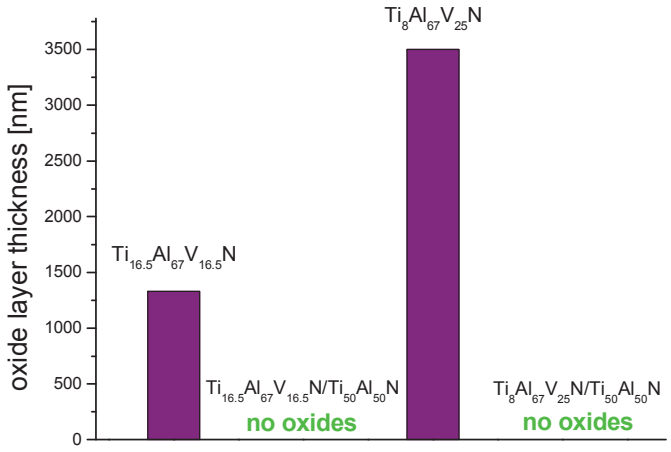

Fig. 4.19 Oxide layer thicknesses of annealed (650 °C; 30 min) single layer coatings alloyed with 16.5 at. % and 25 at. % V, compared to the nearly unaffected multi-layer coatings (named with no oxides). All grown at -40 V bias voltage.

Ti-Al-V-N coatings at -80 V bias voltage

For bias voltages up to -100 V, it has been reported that residual compressive stresses increase due to the higher defect density [39]. This stresses might be responsible for the fracture of many of the -80 V samples annealed.

However, the $Ti_{16.5}Al_{67}V_{16.5}N/Ti_{50}Al_{50}N$ multi-layer coatings do not show any oxide layer formation at -80 V bias. The samples colour also remained the same (grey) as for -40 V bias voltage, but the $Ti_8Al_{67}V_{25}N$ single layer coatings (Fig. 4.20 a) show a major reduction of oxide layer thickness with increased bias voltage and the surface colour changes from some yellow/green tone at -40 V to light grey at -80 V bias voltage. The SEM image in Fig. 4.20 b) can be compared to the -40 V coatings in Fig. 4.18.

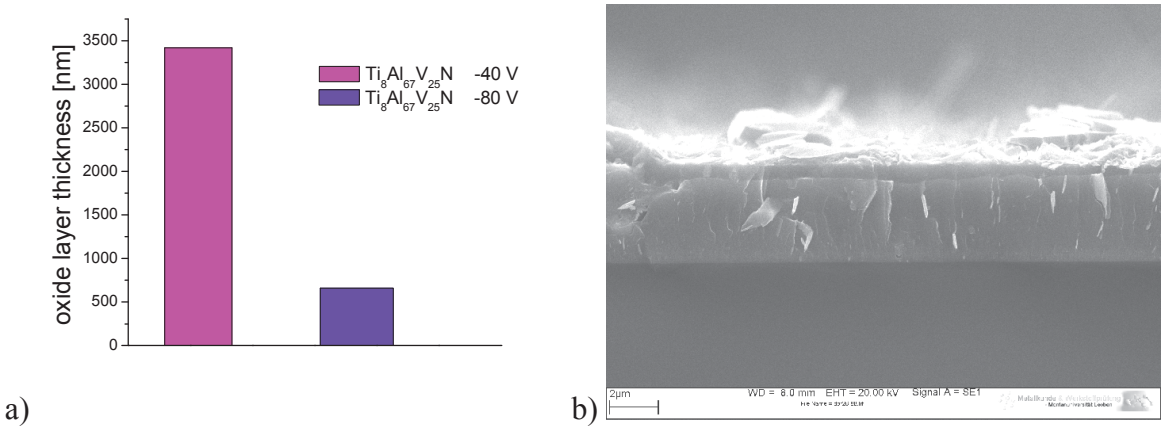

Fig. 4.20 a) Oxide layer thicknesses of annealed $Ti_8Al_{67}V_{25}N$ single layer at -40 V and -80 V bias voltage. b) SEM fracture cross section of an annealed $Ti_8Al_{67}V_{25}N$ single layer coating grown at -80 V bias voltage.

4.4 Wear

Room temperature (RT) and high temperature (HT) (700 °C) tribometer tests were carried out for all coating systems. The wear coefficient was calculated as described in the experimental details section. Wear coefficients of single and multi-layer coatings, for both the -40 V and -80 V bias versions, are compared in this section. The influence of bias voltage and the multi-layer design will be discussed. Structural changes with bias and varying alloying element contents through multi-layer designs are taken into account.

4.4.1 TiAlN coatings

Room temperature

The $Ti_{50}Al_{50}N$ single layer coatings deposited at -40 V and -80 V bias voltage (Fig. 4.21) show lower wear rates as their multi-layer versions (as a combination with $Ti_{33}Al_{67}N$). It has been shown that the wear behaviour of Ti-based coatings at RT is determined by tribochemical reactions of Ti in the presence of moisture and oxygen [87]. Thus, the multi-layer coatings, containing higher amounts of Ti as the single layer versions, show higher wear rates. A coating with a higher amount of interfaces, as it is the case for multi-layers, offers additional paths for the diffusion of species that are involved in the tribochemical reaction. Thus it is conceivable that this yields a higher oxidational wear of multi-layer coatings.

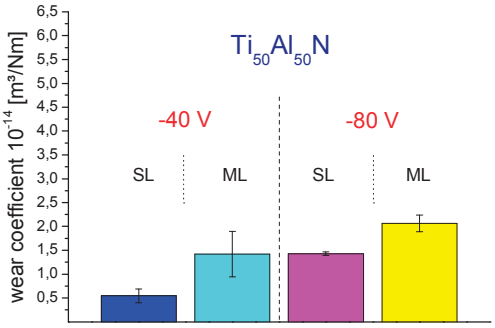

Fig. 4.21 RT wear coefficients of the template material, tested as $Ti_{50}Al_{50}N$ single layer (SL) and $Ti_{33}Al_{67}N/Ti_{50}Al_{50}N$ multi-layer (ML) coatings (-40 V and -80 V bias voltage).

Lower bias voltage and the accompanied lower stresses seem to beneficially influence on the wear behaviour. In contrast to that, higher intrinsic stresses which are accompanied by higher bias voltage might be connected to a change in the chemical potential that also increases the films reactivity, and thus, supports the tribochemical reaction. Furthermore, higher bias

voltage leads to higher amounts of fcc phase fractions, which is also accompanied by multi-layer architecture (see Fig. 4.1). These structural changes can be found reasonable for the different wear coefficients of multi-layer and single layer coatings.

High temperature

The reference coating systems tested at 700 °C show a strong decrease of the wear rate from single to multi-layer film architecture, as Fig. 4.22 shows. Here again, the coatings deposited with higher bias voltage show higher wear, if compared to the coatings of the same architecture. At higher temperatures, the wear behaviour is mainly determined by the oxidation behaviour and the mechanical properties of the coating. The multi-layer architecture shows higher hardness, which can be related to smaller grains (section 4.2). Furthermore, a multi-layer coating system consisting of alternating high and low modulus single layers can better accommodate mechanical deformations and shear stresses than a single layer coating [88]. As a consequence, the multi-layer coatings show a better wear behaviour than the related single layer coatings. Higher bias voltage leads to higher intrinsic stresses as discussed and under mechanical loading, these stresses become detrimental for the coating, and thus, wear increases.

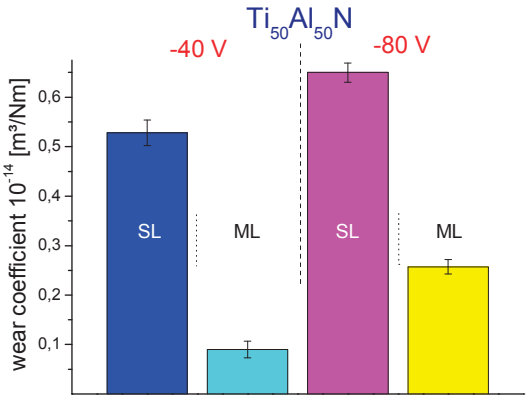

Fig. 4.22 Wear coefficients of the template material $Ti_{50}Al_{50}N$, tested at 700 °C as $Ti_{50}Al_{50}N$ single layer (SL) and $Ti_{33}Al_{67}N/Ti_{50}Al_{50}N$ multi-layer (ML) coatings (-40 V and -80 V bias voltage).

4.4.2 Ti-Al-X-N coatings (X= B, Si, Ta)

Room temperature

Figure 4.23 displays an overview of the wear coefficients of B-, Si-, and Ta alloyed TiAlN coatings at RT. It can be seen that the multi-layer coatings deposited with -40 V bias voltage show the highest wear. As previously mentioned, this might be connected to an increased

tribochemical reaction due to the additional diffusion paths. The lower bias voltage leads to a less dense structure and diffusion might be favoured. Multi-layer design shows higher fcc fractions which should affect positively on the wear behaviour, but this effect does not seem to play the major role for the -40 V coating. Moreover, the overall concentration of Ti in the multi-layers is higher than in the single layer coatings, as the multi-layer consists of alternating $Ti_{50}Al_{50}N$ and alloyed TiAlN layers. A higher overall Ti content would also suggest higher wear for the multilayer deposited at -80 V. However, decreased wear is observed. The reason might be the combined effect of bias voltage and template effect. Thus, this coatings consist solely of fcc structured single layers in contrast to all other coatings that show both fcc and hcp phases. This should be one reason for the better wear behaviour of these coatings. Similarly, the Ta alloyed single layer coating deposited with -80 V bias voltage shows a predominantly fcc structure with no detectable hexagonal phases, and consequently, wear decreases. The B- and Si alloyed single layer coatings behave similar to $Ti_{50}Al_{50}N$ as explained before.

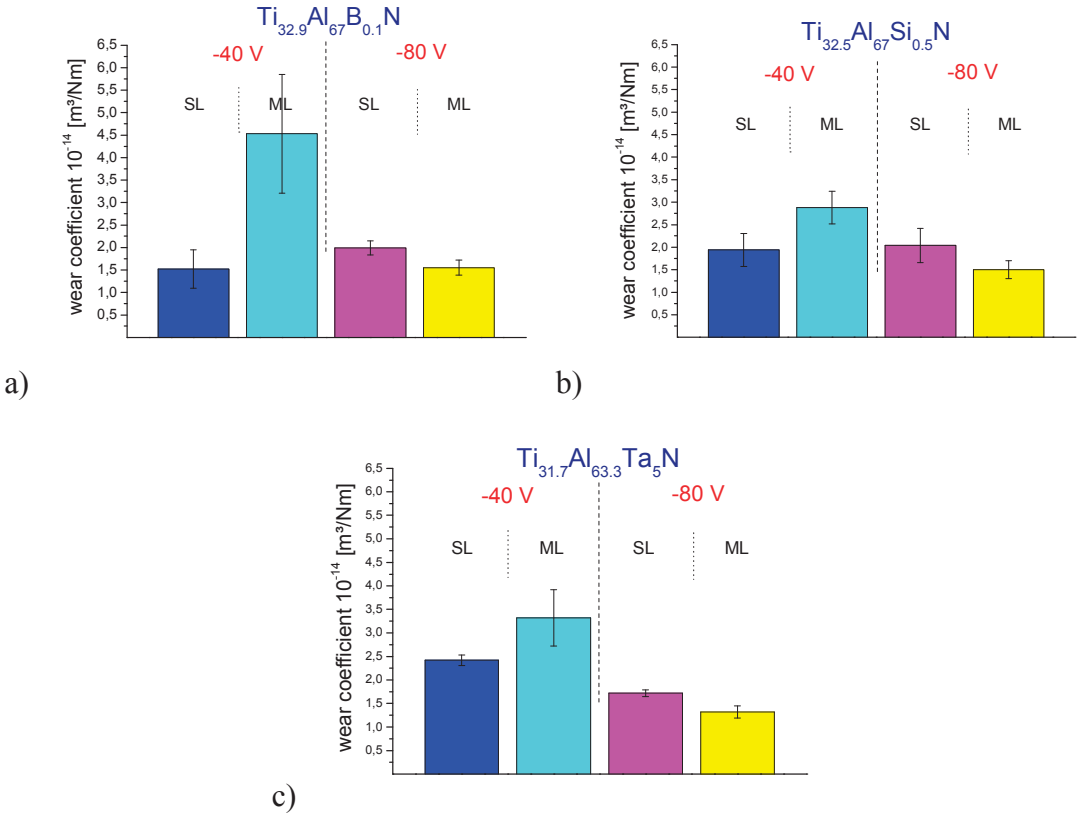

Fig. 4.23 RT wear coefficients of a) B-, b) Si- and c) Ta alloyed single layer (SL) and multi-layer (ML, with a $Ti_{50}Al_{50}N$ template) coatings (-40 V and -80 V bias voltage).

High temperature

Generally, the HT wear tests of B-, Si- and Ta alloyed coatings show lower wear coefficients than observed for RT (cf. Fig. 4.24). On the first sight, there is no clear tendency in the results other than for all three alloying elements the -40 V multi-layer designs show good wear behaviour. Within this group of tested samples, a changing wear mechanism, from adhesive wear to abrasion, has been found to influence the wear rates significantly.

Fig. 4.25 shows 2- and 3 dimensional surface profiles of the wear tracks of B alloyed multi-layer coatings deposited at a) -40 V and b) -80 V bias voltage, and c) Si alloyed multi-layer deposited at -40 V bias voltage. In Fig. 4.25 a), a significant amount of transfer material can be observed. This transfer material originates from both the ball and the surface of the coating. It has been shown for steels that oxide glazes might act as a protective layer and reduce wear, provided that they are mechanically stable [89]. In a similar manner, the material transferred to or formed at the surface of coatings might act protective as well. The wear track of the Ta alloyed multi-layer coating deposited with -40 V bias looks the same as illustrated in Fig. 4.25 a), and thus shows low wear.

Fig. 4.25 b) indicates the presence of abrasive wear as main wear mechanism. For all coatings where abrasive wear is the main mechanism, wear is high. This is the case for all single layers and for the Ta- and B alloyed multi-layer coatings deposited with -80 V bias. There seems to be a transition from adhesive to abrasive wear for some coatings, and the appearance of the wear track is similar to that illustrated in Fig. 4.25 c). Here, both transferred material and ploughs can be seen. As a consequence, these coatings show an increase in wear compared to the coatings where adhesive wear is the main mechanism.

There are still some particularities in the results that should be discussed. The Si alloyed multi-layer coating deposited with -80 V bias shows less wear than the one deposited with -40 V bias. The reason is that adhesive wear is more pronounced in the former. The Ta alloyed single layer deposited with -80 V bias shows a lower wear coefficient as the -40 V single layer. This behaviour could be explained with its increased mechanical properties due to bias related change from a dual phase structure (hcp + fcc) to a nearly fcc single phase structure. However, the main reason for the decrease in wear is connected to a change in wear mechanism, from abrasive to a mixture of adhesive and abrasive wear. It is not yet clear in which way there is a connection between coatings structure and wear mechanisms. More precisely, it is not yet clear, why the Ta- and B alloyed multi-layer coatings show abrasive wear. The only visible difference is that Young's moduli of the Si alloyed multi-layer coatings increase with increasing bias, while those of the Ta- and B alloyed multi-layer coatings decrease (cf. Fig. 4.8-4.11). This might have an influence in the mechanical response of the coatings under loading that leads to the unexpected change in the wear mechanism.

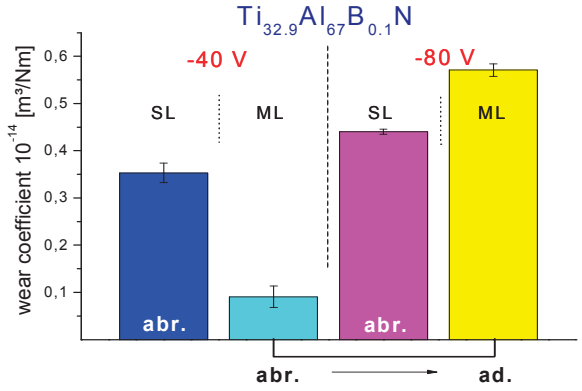

a)

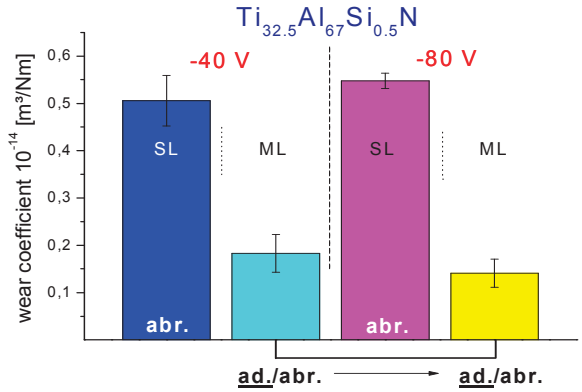

b)

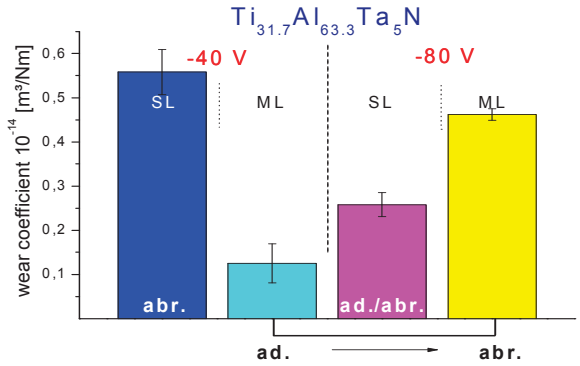

c)

Fig. 4.24 Wear coefficients after tribological tests at 700 °C of a) B-, b) Si- and c) Ta alloyed TiAlN single layer (SL) and multi-layer (ML, with a $Ti_{50}Al_{50}N$ template) coatings grown at -40 V and -80 V bias voltage. Adhesive wear mechanism (ad.), abrasive wear mechanism (abr.) and the transition state (ad./abr.).

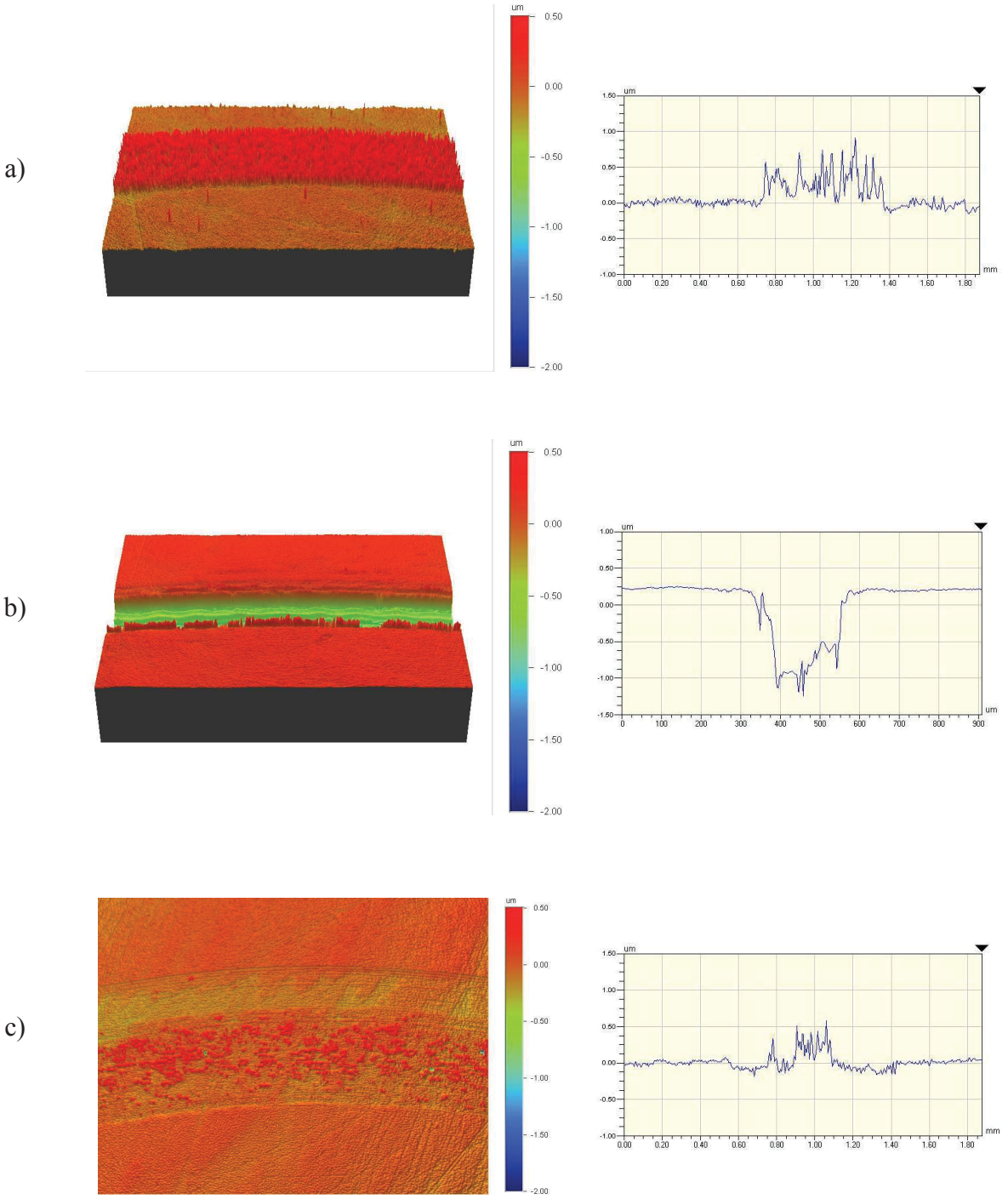

Fig. 4.25 3D and 2D surface profiles of wear tracks showing a) dominating adhesive wear ($Ti_{32.9}Al_{67}B_{0.1}N/Ti_{50}Al_{50}N$ multi-layer, -40 V), b) dominating abrasive wear ($Ti_{32.9}Al_{67}B_{0.1}N/Ti_{50}Al_{50}N$ multi-layer, -80 V), and c) the transition state between adhesive and abrasive wear ($Ti_{32.5}Al_{67}Si_{0.5}N/Ti_{50}Al_{50}N$ multi-layer, -40 V).

4.4.3 Ti-Al-V-N coatings

Room temperature

Fig. 4.26 displays the wear coefficients after tribological tests at RT of V alloyed coatings containing a) 16.5 at. % and b) 25 at. % V. It can be seen that the single layer coatings show a better wear resistance than the multi-layer coatings. Here again, the higher wear of the multi-layer coatings might be related to their higher Ti content compared to the single layer coatings, and the additional diffusion paths for species involved in the tribochemical attack. The lower Ti content of the coatings containing of 25 at. % V might be also the reason why these coatings show a better wear behaviour than the analogous coatings containing 16.5 at. % of V. If the two multi-layer coatings alloyed with 16.5 at. % of V are compared, the -80 V version shows better wear resistance. This can be related to the single phase fcc structure of the multi-layer grown at -80 V bias voltage in comparison to the fcc and hcp containing two phase structure of the one grown at -40 V bias voltage. In case of the coatings with a V content of 25 at. %, there seems to be no influence of bias voltage in the wear behaviour of analogous coatings.

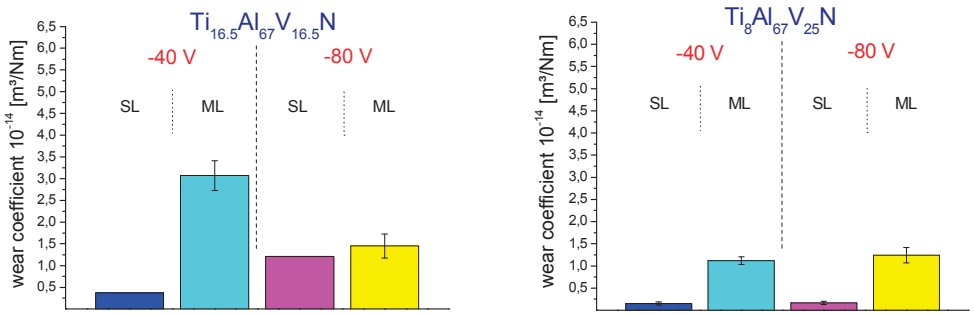

a) b)

Fig. 4.26 RT wear coefficients of, a) $Ti_{16.5}Al_{67}V_{16.5}N$ and b) $Ti_8Al_{67}V_{25}N$ single layer (SL) and multi-layer (ML, with a $Ti_{50}Al_{50}N$ template) coatings (-40 V and -80 V bias voltage).

High temperature

The only V containing coatings that withstood the tribo-tests at 700 °C were the multi-layers containing 16.5 at. % of V. Their wear coefficients are displayed in Fig. 4.27. At 700 °C there is an out-diffusion of V atoms to the surface, and a very strong oxidation of the single layer coatings, as previously explained in chapter 4.3.2, that yields a mechanical instability of the coatings, and ultimately coating failure. For the multi-layers containing 16.5 at. % V, it is conceivable that the $Ti_{50}Al_{50}N$ layers act as a barrier and hinder the out-diffusion of V atoms and the in-diffusion of O atoms. This mechanism is not effective in case of the multi-layer coatings containing 25 at. % V, and then, they failed as well. The wear behaviour of the V alloyed coatings is thus determined by their oxidation behaviour. In this respect, it might be possible that the higher stresses in the multi-layer coating deposited with -80 V bias has a negative influence on the oxidation behaviour that could not be measured during the oxidation experiments thus yielding a higher wear of this coating.

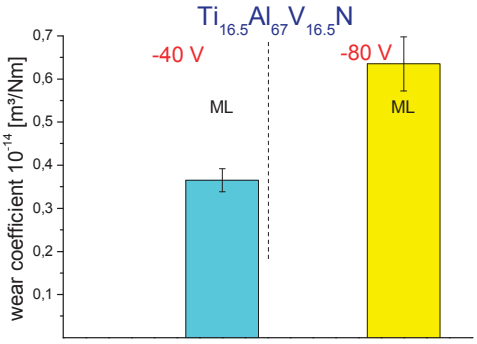

Fig. 4.27. Wear coefficients of $Ti_{16.5}Al_{67}V_{16.5}N/Ti_{50}Al_{50}N$ multi-layer (ML) coatings (-40 V and -80 V) after tribological tests at 700 °C.

5 Summary and conclusions

This thesis has been carried out to investigate similarities and differences of alloyed cathodic arc evaporated single and multi-layer coatings. B, Si, Ta and two different concentrations of V have been alloyed to the ternary TiAlN coating system based on the $Ti_{33}Al_{67}N$ composition. In case of multi-layer architecture, $Ti_{50}Al_{50}N$ has been used as a second layer (template). All coatings have been grown by cathodic arc evaporation at -40 V and -80 V bias voltage.

Structural investigations (XRD) gave information on the change of phase contents by alloying, biasing and multi-layering. It was found that the fcc phase can be promoted through appliance of higher bias voltage or multi-layering. Concerning the alloying elements, Si and B pushed the coating systems' structure to higher hcp phase fractions, while in contrast to that Ta and V did promote the fcc phase on the expense of the hcp phase. Higher bias voltages affected the structure with a shift to higher fcc phase contents and a smaller grain size. Multi-layering led to higher contents of fcc phases, which was provided by the introduction of an fcc template layer, where the growth of fcc phases was favoured (template effect). Furthermore, it has been shown that all these effects can occur in addition and are possible within single and multi-layer coatings (except from the template effect, which is related solely to multi-layer coatings).

Ongoing from structure, the mechanical properties showed to mainly depend on the phase composition and the layer architecture. High hardness could be related to high fcc phase fractions and small grain size (Hall Petch effect). This has been achieved by higher bias voltage, which caused higher fcc phase fractions and a smaller grain size as already mentioned. Hardness has also been increased by multi-layering, while an fcc single phase template layer provided higher fcc phase fractions within the multi-layers' phase composition. Thus multi-layering enabled the increase of hardness at lower bias voltages, which allowed to end up with the same benefits while residual stresses were kept low. It was shown, that these two effects can act in an additive way. In case one effect is not able to prevent hcp phases, the second one can be used to further decrease the hcp phase.

The Young´s modulus of single layer coatings has been found to increase with the bias voltage, which is related to a decreased hcp phase. For the multi-layer design, the Young´s modulus decreases with higher bias voltage. This has been related to the formation of additional interfaces and the following increase of deformation possibilities.

Oxidation tests have been carried out at 900 °C for 60 min in case of the B-, Si- and Ta alloyed coatings. Due to their lower oxidation resistance, annealing conditions of V alloyed samples have been set to 650 °C and 30 min. After annealing in air, oxide layer thicknesses have been investigated to function as indicators for oxidation resistance. It could be found that V single layer designs do oxidize heavily and that V multi-layers do have improved oxidation

resistance due to the $Ti_{50}Al_{50}N$ template layer. Higher V contents cause higher oxidation rates, but have been observed to be also dramatically improved for multi-layers in the employed temperature range.

B-, Si- and Ta alloyed coatings showed improved oxidation behaviour compared to the unalloyed TiAlN coatings. In case of Si, multi-layering led to a further improvement of the oxidation behaviour and this could be related to the stronger change in structure from a higher hcp phase content to the almost sole fcc structure at higher applied bias voltage.

In contrast to that, Ta alloying of the films did not affect the oxidation resistance heavily between single and multi-layer design and showed an even lower oxidation resistance for the multi-layer coating. In this case the template effect is of minor importance due to a higher fcc phase content already introduced by Ta alloying. The lower Ta content of the multi-layer coating seemed to be responsible for its lower oxidation resistance compared to the single layer film.

Except from Ta with its already excellent effect on oxidation resistance, it can be concluded that multi-layering has a positive effect on the oxidation resistance of all coatings and that bias voltage can lead to higher stresses which can be harmful for oxidation resistance.

At RT, tribo-chemical reactions of Ti in the presence of moisture has been found to be the determinant wear mechanism. In this regard, a multi-layer architecture that has higher Ti contents through the $Ti_{50}Al_{50}N$ template layer has also higher wear rates at RT. Here, higher bias voltage and the accompanied higher stresses can induce a higher chemical reactivity of the coatings, ending up in a higher wear rate. It could also be shown that a highly cubic structure shows better wear behaviour.

At high temperatures, mainly the mechanical and oxidation properties of the coatings determine their wear behaviour. Referring to this, multi-layer architecture provides advantages compared to single layer architecture. When a change in the dominating wear mechanism from adhesive to abrasive wear occurs due to the mechanical response of the coatings, wear increases significantly. In case of the V containing coatings, the wear behaviour at high temperatures is determined by the oxidation behaviour of the coating; the better the oxidation behaviour, the better is also the wear behaviour.

Generally, multi-layering has a beneficial effect on structure, mechanical properties and oxidation resistance. In case of V alloyed coatings, multi-layering generates diffusion barriers which are of major importance to provide higher oxidation resistance. Alloying of B, Si and Ta in TiAlN multi-layer coatings grown at -40 V bias voltage had beneficial effects on the oxidation resistance and the wear behaviour at high temperatures. This was not found for the samples grown at -80 V bias voltage, where the wear mechanism changed. Higher bias voltage did on the one hand lead to higher induced stresses, accompanied by higher wear rates and on the other hand, the higher bias voltage led to improved structure, mechanical properties and oxidation resistance.

6 References

[1] S. PalDey, S.C. Deevi, Mat. Sci. Eng. A342 (2003) 58.

[2] R.K. Waits, The 46th international symposium of the american vacuum society, AVS, Seattle, Washington (USA), 2000, p. 1736.

[3] F.W. Bach, A. Laarmann, T. Wenz, Modern Surface Technology, Wiley-VCH Verlag GmbH, Weinheim, 2006.

[4] K.M. Mertz, H.A. Jehn, Praxishandbuch moderne Beschichtungen - Advanced surface coatings, Carl Hanser Verlag München Wien, 2001.

[5] W. Gissler, H.A. Jehn, Advanced Techniques for Surface Engineering, Kluwer Academic Publishers, Dordrecht, 1992.

[6] G. Kienel, K. Röll, Vakuum Beschichtung 2, VDI Verlag, Düsseldorf, 1995.

[7] B. Rother, J. Vetter, Plasma-Beschichtungsverfahren und Hartstoffschichten, Dt. Ver. für die Grundstoffindustrie, Leipzig, 1992.

[8] R.A. Haefer, Oberflächen und Dünnschichttechnologie, Springer Verlag, Berlin, 1987.

[9] F.W. Bach, T. Duda, Moderne Beschichtungsverfahren, Wiley-VCH Verlag GmbH, Weinheim, 2000.

[10] J.L. Vossen, W. Kern, Thin Film Processes II, Academic Press, San Diego, 1991.

[11] G. Franz, Oberflächentechnologie mit Niederdruckplasmen, Springer Verlag, Berlin, 1994.

[12] E. Lugscheider, K. Bobzin, C. Barimani, S. Bärwulf, T. Hornig, Ad. Eng. Mat. 2 (1-2) (2000) 33.

[13] R. Franz, Personal Communication (2008).

[14] D.M. Sanders, A. Anders, Surf. Coat. Technol. 133-134 (2000) 78.

[15] J. Wagner, Diploma Thesis, Montanuniversität of Leoben, Leoben, 2003.

[16] P.B. Barna, Diagnostics and Applications of Thin Films, Bristol, 1992.

[17] B.A. Movchan, A.V. Demchishin, Phys. Met. Metallogr. 28 (1969) 83.

[18] J.E. Greene, Handbook of Crystal Growth, Elsevier, Amsterdam, 1993.

[19] http://ipap.yonsei.ac.kr/~fenian/semiconductor.htm, (12.07.2008).

[20] M. Ohring, The Materials Science of Thin Films, Academic Press, San Diego, 1992.

[21] J.A. Thornton, J. Vac. Sci. Technol. 11 (4) (1974) 666.

[22] R. Messier, A.P. Giri, R.A. Roy, J. Vac. Sci. Technol. A2(2) (1984) 500.

[23] H.A. Jehn, B. Rother, Int. J. Ref. Met. & Hard Mat. 14 (1995) 87.

[24] S. PalDey, S.C. Deevi, Mat. Sci. Eng. A361 (2003) 1.

[25] W.D. Münz, J. Vac.Sci. Technol. Vol 4/No 6 (1986) 2717.

[26] R. Cremer, M. Witthaut, D. Neuschuetz, TMS Annual Meeting (1998) 249.

[27] A. Kimura, H. Hasegawa, K. Yamada, T. Suzuki, J. Mat. Sci. Lett. 19 (2000) 601.

[28] http://www.pvd-coatings.co.uk/theory.htm, (11.08.2008).

[29] H. Holleck, Surf. Coat. Technol. 36 (1-2) (1988) 151.

[30] P. Spencer, Z. Metallkunde 92 (10) (2001) 1145.

[31] P.H. Mayrhofer, F.D. Fischer, H.J. Böhm, C. Mitterer, J.M. Schneider, Act. Mat. 55 (4) (2007) 1441.

[32] M. Zhou, Y. Makino, M. Nose, K. Nogi, Thin Solid Films 339 (1999) 203.

[33] H. Willmann, PhD Thesis, Montanuniversität Leoben, Leoben, 2007.

[34] M. Moser, PhD Thesis, Montanuniversität Leoben, Leoben, 2008.

[35] K. Sato, N. Ichimiya, A. Kondo, Y. Tanaka, Surf. Coat. Technol. 163-164 (2003) 135.

[36] H. Ljungcrantz, L. Hultman, J.E. Sundgren, L. Karlsson, J. Appl. Phys. 78 (2) (1995) 832.

[37] S. PalDey, S.C. Deevi, T.L. Alford, Intermetallics 12 (7-9) (2004) 985–991.

[38] I. Petrov, P.B. Barna, L. Hultman, J.E. Greene, J. Vac. Sci. Technol. A 21 (5) (2003) 117.

[39] M. Pfeiler, K. Kutschej, M. Penoy, C. Michotte, C. Mitterer, M. Kathrein, Surf. Coat. Technol. 202 (2007) 1050.

[40] A. Hörling, L. Hultman, M. Odén, J. Sjölén, L. Karlsson, J. Vac. Sci. Technol. A 20 (5) (2002) 1815.

[41] P.H. Mayrhofer, A. Horling, L. Karlsson, J. Sjolen, T. Larsson, C. Mitterer, L. Hultman, Appl. Phys. Lett. 83 (10) (2003) 2049.

[42] W.S. Gwidon, A.W. Batchelor, Engineering Tribology, Butterworth-Heinemann, Woburn, 2001.

[43] K. Kutschej, P.H. Mayrhofer, M. Kathrein, P. Polcik, C. Mitterer, Surf. Coat. Technol. 188-189 (2004) 358.

[44] K. Kutschej, C. Mitterer, C.P. Mulligan, D. Gall, Ad. Eng. Mat. 8 (11) (2006) 1125.

[45] P.C. Jindal, A.T. Santhanam, U. Schleinkofer, A.F. Shuster, Int. J. Ref. Met. & Hard Mat. 17 (1) (1999) 163.

[46] P.H. Mayrhofer, Personal Communication (2008).

[47] G.A. Fontalvo, Personal Communication (2008).

[48] J.D. Bressan, R. Hesse, E.M. Silva Jr., Wear 250 (2001) 561.

[49] J.H. Hsieh, C. Liang, C.H. Yu, W. Wu, Surf. Coat. Technol. 108-109 (1998) 132.

[50] J.R. Davis, Surface engineering for corrosion and wear resistance, ASM International, Materials Park, 2001.

[51] O. Knotek, W.D. Münz, T. Leyendecker, J. Vac. Sci. Technol. A5 (4) (1986) 2173.

[52] W. D. Münz, J. Vac. Sci. Technol. A4 (6) (1986) 2717.

[53] I. Wadsworth, I.J. Smith, L.A. Donohue, W.D. Münz, Surf. Coat. Technol. 94-95 (1997) 315.

[54] M. Moser, P.H. Mayrhofer, Scr. Mat. 57 (2007) 357–360.

[55] O. Durand-Drouhin, A.E. Santana, A. Karimi, V.H. Derflinger, A. Schütze, Surf. Coat. Technol. 163-164 (2003) 260.

[56] S. Veprek, M.J.G. Veprek-Heijman, Surf. Coat. Technol. 202 (21) (2008) 5063.

[57] M.A. Baker, S. Klose, C. Rebholz, A. Leyland, A. Matthews, Surf. Coat. Technol. 151-152 (2002) 338.

[58] C. Rebholz, A. Leyland, A. Matthews, Thin Solid Films 343-344 (1999) 242.

[59] M. Pfeiler, G.A. Fontalvo, J. Wagner, K. Kutschej, M. Penoy, C. Michotte, C. Mitterer, M. Kathrein, Tribol. Lett. 30 (2) (2008) 91.

[60] M. Kathrein, C. Michotte, M. Penoy, P. Polcik, C. Mitterer, Surf. Coat. Technol. 200 (5-6) (2005) 1867.

[61] C. Mitterer, Lecture Script: Nanostrukturierte Werkstoffe (2007).

[62] C. Ducros, C. Cayron, F. Sanchette, Surf. Coat. Technol. 201 (2006) 136.

[63] U. Helmersson, S. Todorova, S.A. Barnett, J.E. Sundgren, L.C. Markert, J.E. Greene, J. Appl. Phys. 62 (2) (1987) 481.

[64] J.G. Han, K.H. Nam, I.S. Choi, Wear 214 (1) (1998) 91.

[65] H.G. Prengel, P.C. Jindal, K.H. Wendt, A.T. Santhanam, P.L. Hegde, R.M. Penich, Surf. Coat. Technol. 139 (1) (2001) 25.

[66] K.N. Andersen, E.J. Bienk, K.O. Schweitz, H. Reitz, J. Chevallier, P. Kringhøj, J. Bøttiger, Surf. Coat. Technol. 123 (2-3) (2000) 219.

[67] V.H. Derflinger, A. Schütze, M. Ante, Surf. Coat. Technol. 200 (16-17) (2006) 4693.

[68] B.D. Cullity, Elements of X-Ray diffraction, Addison-Wesley Publishing Company INC., London, 1978.

[69] A.C. Fischer Cripps, The IBIS Handbook of Nanoindentation, Fischer-Crips Laboratories Pty Ltd, Forestville Australia, 2005.

[70] DIN EN ISO 14577-1, 2003.

[71] DIN EN ISO 14577-2, 2003.

[72] DIN EN ISO 14577-3, 2003.

[73] G. Gassner, Diploma Thesis, Montanuniversität Leoben, Leoben, 2003.

[74] Veeco, Metrology Group, WYCO Surface Profilers Technical Reference Manual Tucson (1999).

[75] K. Kutschej, B. Rashkova, J. Shen, C. Edwards, C. Mitterer, G. Dehm, Thin Solid Films 516 (2007) 369.

[76] K. Kutschej, N. Fateh, P.H. Mayrhofer, M. Kathrein, P. Polcik, C. Mitterer, Surf. Coat. Technol. 200 (1-4) (2005) 113.

[77] M. Pfeiler, J. Zechner, M. Penoy, C. Mitterer, M. Kathrein, Surf. Coat. Technol. in Submission (2008).

[78] F. Vaz, L. Rebouta, M. Andritschky, M.F. Silva, J.C. Soares, Surf. Coat. Technol. 98 (1998) 912.

[79] S.J. Bull, The 47th international symposium: Vacuum, thin films, surfaces/interfaces, and processing NAN06, AVS, Boston, Massachusetts (USA), 2001, p. 1404.

[80] Y. Long, F. Giuliani, S.J. Lloyd, J. Molina-Aldareguia, Z. H. Barber, W. J. Clegg, Composites Part B: Engineering 37 (6) (2006) 542.

[81] G. Gottstein, Physikalische Grundlagen der Metallkunde, Springer Verlag Berlin Heidelberg 2001.

[82] K. Kutschej, P.H. Mayrhofer, M. Kathrein, C. Michotte, P. Polcik, C. Mitterer, in: G. Kneringer, P. Roedhammer, H. Wildner (Eds.), Plansee Seminar, Reutte Austria, 2005.

[83] J.R. Roos, J.P. Celis, E. Vancoille, H. Veltrop, S. Boelens, F. Jungblut, J. Ebberink, H. Homberg, Thin Solid Films 193-194 (1) (1990) 547.

[84] Y. Tanaka, T.M. Gür, M. Kelly, S.B. Hagstrom, T. Ikeda, K. Wakihira, H. Satoh, J. Vac. Sci. Technol. A 10 (4) (1992) 1749.

[85] J. Zechner, Diploma Thesis, Montanuniversität Leoben, Leoben, 2008.

[86] R. Franz, J. Neidhardt, C. Mitterer, B. Schaffer, H. Hutter, R. Kaindl, B. Sartory, R. Tessadri, M. Lechthaler, P. Polcik, J. Vac. Sci. Technol. A: Vacuum, Surfaces, and Films 26 (2) (2008) 302.

[87] M. Pfeiler, K. Kutschej, M. Penoy, C. Michotte, C. Mitterer, M. Kathrein, Int. J. of Ref. Met. & Hard Mat./in press (2008).

[88] A. Matthews, S. Franklin, K. Holmberg, J. Phys. D: Appl. Phys. 40 (18) (2007) 5463.

[89] G.A. Fontalvo, C. Mitterer, Wear 258 (10) (2005) 1491.